University of Minnesota
St. Anthony Falls Hydraulic Laboratory
Department of Civil & Mineral Engineering
Mississippi River at 3rd Avenue S.E.
Minneapolis, Minnesota

Project Report No. 261

HYDRODYNAMIC ANALYSIS OF THE HYKAT

Final Report

by

Charles C. S. Song, Joseph M. Wetzel,

M. Yuan, Roger E. A. Arndt, and John M. Killen

Prepared for

Hamburgische Schiffbau-Versuchsanstalt
Hamburg, West Germany

June 1987

TABLE OF CONTENTS

HYDRODYNAMIC ANALYSIS OF THE HYKAT

I. INTRODUCTION

The St. Anthony Falls Hydraulic Laboratory has carried out a hydrodynamic analysis of several critical components of a preliminary design configuration of the HYKAT. A sketch of this configuration is shown in Fig. 1. The components subjected to detailed analysis were those of the upper leg, including the contraction, turning vanes of the first elbow, and the turbulent management system. Head loss computations were made for the entire flow circuit. Mathematical modeling was used extensively for analysis of the contraction and the turning vanes. Based on the results of this study, recommendations have been made for some modification to the preliminary design. Some of the results presented here have been previously included in progress reports, and results of additional studies are summarized.

II. DESCRIPTION OF MATHEMATICAL MODEL

Until quite recently the analysis of large Reynolds number flows, such as the flows in contraction and turning vanes, were largely based on the potential flow theory. The current trend is to replace the potential flow model with an Euler equation model so that the effect of vorticity can be included in the analysis. Because the inflow velocity profiles for the contraction and the turning vanes are likely to be nonuniform, an Euler equation model was chosen for this work.

A steady flow problem can be solved equally well with a steady flow model or an unsteady flow model. An unsteady flow model was chosen for this project because it is more general and the same model can be used if it is decided in the future to study the sensitivity of the turning vanes to the time-dependent turbulence eddies. Numerical analysis of incompressible flows based on the Euler equations is rather difficult due to the elliptic nature of the equation of continuity. A usual compressible flow model is notoriously inefficient at small Mach numbers. For this reason the St. Anthony Falls Hydraulic Laboratory has developed a weakly compressible flow model which has been successfully applied in other projects. The weakly compressible flow model used for this project is briefly described below.

The equation of continuity for a barotropic flow can be written as

$$\frac{\partial p}{\delta t} + (\vec{V}\cdot\nabla)p + a^2\rho\nabla \cdot \vec{V} = 0 \qquad (1)$$

in which p is the pressure, a is the speed of sound, and ρ is the density. For an incompressible fluid, $a \to \infty$, and Eq. 1 degenerates into

$$\nabla \cdot \vec{V} = 0 \qquad (2)$$

The change from Eq. 1 to Eq. 2 is so drastic that Eq. 2 is not valid for highly time-dependent real fluid flow. The difference between Eq. 1 and 2 is much like the difference between the Navier-Stokes equation and the Euler equation.

When Eq. 1 is written in dimensionless form, it becomes clear that the second term is proportional to the square of the Mach number and, hence, can be neglected if the Mach number is small. On the other hand, the first term is proportional to the Strouhal number times the square of the Mach number and, hence, may not be neglected when the Strouhal number is large. The continuity equation for a weakly compressible fluid is, by neglecting the second term in Eq. 1, as follows:

$$\frac{\partial p}{\partial t} + a^2 \rho \, \nabla \cdot \vec{V} = 0 \tag{3}$$

By weakly compressible flow, it also means that a and ρ in Eq. 3 are treated as constants. The corresponding equation of motion for weakly compressible, inviscid fluid is

$$\frac{\partial \vec{V}}{\partial t} + (\vec{V} \cdot \nabla) \cdot \vec{V} + \nabla\left(\frac{p}{\rho}\right) = 0 \tag{4}$$

Eq. 4 is actually the Euler equation for the incompressible fluid. It is not difficult to show that this equation is also accurate to the second order of Mach number.

The weakly compressible Euler equation model used for this project is based on Eqs. 3 and 4. When this model is used to solve a steady flow problem, the converged solution is identical to that of an incompressible fluid. This is true since in the limiting case of $\partial / \partial t \to 0$, Eq. 3 reduces to Eq. 2. A rapid convergence method recently developed at the St. Anthony Falls Hydraulic Laboratory, whose convergence speed is independent of the Mach number and faster than most other methods, was used for some later runs.

III. RESULTS OF MATHEMATICAL MODELING

A. Contraction

Based on the previous experience with the design of the Large Cavitation Channel (LCC), the fifth-order polynomial contraction was selected. This profile is more flexible and smoother than the commonly used matched third order polynomial profile. The contraction matches the entrance section and the test section in terms of the position, slope, and the curvature. In addition, the inflexion point can be varied to minimize the potential for boundary layer separation and cavitation.

A number of geometrical parameters were varied in search of the most desirable configuration. The completed simulation runs are listed below.

Run No. 1: This is the base line run using the dimensions suggested by Kempf and Remmers, as shown in Fig 1. The contraction is 7.7 m long and the top surface is flat. The inflexion point is located 60% from the exit. Because of symmetry, only half of the field was modeled.

Run No. 2: The inflexion point is moved to the 65% point from the exit. All other dimensions remain the same as that of Run No. 1. This is a half model.

Run No. 3: The contraction length is increased by 1 m (total length 8.7 m). All other dimensions remain the same as that of Run No. 1. This is a half model.

Run No. 4: The contraction exit is changed to a 2.12 m x 2.12 m square. All other dimensions remain the same as that of Run No. 1. This is a half model.

Run No. 5: The contraction is made symmetrical by lowering the exit. Contraction in the vertical direction is shared equally by the top surface and the bottom surface. All other dimensions remain the same as that of Run No. 1. Only 1/4 of the flow field is modeled.

Run No. 6: Repeat of Run No. 3 using the total flow field in the simulation. For all previous five runs, only part of the flow field was computed by invoking the symmetry condition.

Run No. 7: This is a repeat of Run No. 5 except that the contraction is 1 m longer and the full field is modeled.

Run No. 8: This run is the same as Run No. 6 except that a nonuniform inflow velocity distribution is used. A trapizoidal velocity profile with maximum velocity at the bottom which is 20 percent greater than the mean velocity was used.

Run No. 9: This run is the same as Run No. 7 except that the nonuniform inflow velocity distribution of Run No. 8 is used.

Run No. 10: A nonsymmetrical contraction for which the vertical position of the contraction exit is located midway between the flat top case and the symmetrical case was assumed. Uniform inflow velocity distribution was used.

Run No. 11: The nonuniform inflow velocity distribution was used for the contraction geometry of Run No. 10.

The computed pressure coefficient, using the mean pressure and velocity at the test section as the reference values, along three streamlines on a side wall of Run No. 1 are plotted in Fig. 2. The largest negative pressure is observed near the exit at the bottom corner as indicated by line 3. A small amount of adverse pressure gradient also exists at the bottom corner near the entrance. Computed pressure coefficients along three streamlines on the vertical plane of symmetry are plotted in Fig. 3. Application of Stratford boundary layer separation criterion indicates no tendency for boundary layer separation to occur in this contraction.

The computed pressure coefficient along the same six streamlines for Run No. 3 are plotted in Figs. 4 and 5. Significant improvement of the pressure distribution is obtained by increasing the contraction length by 1 m. Similar plots for Run No. 7 are shown in Figs. 6 and 7. Very substantial improvement on pressure distribution for symmetrical contraction over asymmetrical contraction is indicated.

The velocity vector field on the cross-sectional plane at the exit calculated for Run No. 7 is shown in Fig. 8. A weak secondary current in the general direction of bottom to top and side to center exists on this plane. This secondary current caused by the contraction persists in the the test section. Previous investigation for the LCC indicated that the secondary current contributes to velocity nonuniformity in the test section. As shown in Fig. 8, the maximum value of the secondary current at the exit is 2.8×10^{-4} times the longitudinal velocity.

Some useful flow quality parameters for all runs completed are summarized in Table 1. Columns 6 and 7 list the velocity nonuniformity parameters at the entrance and the exit, respectively. The first seven runs indicate that the contraction distorts the velocity distribution by modest amounts when the inflow velocity is uniform. Column 8 represents the percentage difference between the mean velocity and minimum velocity at the exit. The reason why the values in Column 7 are larger than the corresponding values in Column 8 is that the above average velocity occurs only in two small areas at the bottom corners. The velocity distribution in the remaining area, excluding two small areas at the bottom corners, is quite uniform.

Run Nos. 8, 9, and 11, were made to test the effectiveness of the contraction in correcting nonuniform velocity imposed at the entrance. A linear velocity profile, with its maximum located at the bottom and 20 percent greater than the average, is used as the inflow velocity for these runs. The results show that the contraction is very effective in improving the quality of velocity profiles.

TABLE 1

1	2	3	4	5	6	7	8	9	10
Run No.	Field Modeled	Contraction length m	$\frac{L_d}{L}$	Test Section	Inflow $\frac{u_{max}-\bar{u}}{\bar{u}}$, %	Outflow $\frac{u_{max}-\bar{u}}{\bar{u}}$, %	Outflow $\frac{\bar{u}-u_{min}}{\bar{u}}$, %	Min C_p	percent improvement on C_p
1	half	7.7	0.6	2.8x1.6	0	0.69	0.27	-0.1131	--
2	half	7.7	0.65	2.8x1.6	0	0.95	0.60	-0.0992	12
3	half	8.7	0.6	2.8x1.6	0	0.86	0.176	-0.0847	25
4	half	7.7	0.6	2.12x2.12	0	0.94	0.62	-0.1207	-6.7
5	quarter	7.7	0.6	2.8x1.6	0	1.1	0.58	-0.0375	67
6	full	8.7	0.6	2.8x1.6	0	0.29	0.30	-0.0851	25
7	full	8.7	0.6	2.8x1.6	0	0.91	0.50	-0.0219	81
8	full	8.7	0.6	2.8x1.6	20	1.72	1.47	-0.0890	21
9	full	8.7	0.6	2.8x1.6	20	2.37	1.30	-0.0319	72

Figure 9 shows how the initially uniform velocity profile is being modified by the nonsymmetrical contraction. In the entrance region upstream of the inflexion point, velocity increases more rapidly at the top than the bottom. The trend reverses in the region downstream of the inflexion point. In the end, the maximum velocity occurs at the bottom for the L_d/L equal to 0.6 case.

Figure 10 is a similar plot for the symmetrical contraction. The center plane of the symmetrical contraction is equivalent to the top surface of the nonsymmetrical contraction and, therefore, the maximum occurs at the boundaries and the minimum occurs at the center of the exit.

Figure 11 shows how the nonuniform inflow is being modified by the nonsymmetrical contraction. Because the maximum inflow occurs at the bottom and, as indicated by Fig. 9, the contraction tends to produce higher velocity at the bottom even with uniform inflow, there is an increased nonuniformity as compared with Fig. 9. Figure 12 shows the case when a similar nonuniform inflow is imposed on the symmetrical contraction. In this case the maximum occurs at the side of maximum inflow and the minimum occurs at the center.

Boundary layer computations were also carried out for the symmetrical contraction and the nonsymmetrical contraction. The displacement thickness for laminar boundary layer at the contraction exit is very small for each case computed. They are listed below:

TABLE 2. Displacement Thickness at Contraction Exit

Symmetrical contraction, top and bottom	1.26 mm
Nonsymmetrical contraction, top	2.5 mm
Nonsymmetrical contraction, bottom	3.4 mm

Turbulent boundary layer computations were not carried out because of time constraints.

The three alternatives compared are (1) the nonsymmetrical design with flat top, (2) intermediate design with 1/3 contraction from the top and 2/3 contraction from the bottom, and 3) symmetrical contraction. The basis for the comparison are (1) cavitation characteristics, (2) velocity uniformity, and (3) boundary layer characteristics.

It turned out that all three alternatives are almost equally good in terms of velocity uniformity and boundary layer characteristics. Considering the pressure coefficient distribution as computed by the mathematical model and the hydrostatic pressure, it is possible to determine the position of maximum cavitation susceptibility. It is desirable not to have cavitation occurring in other parts of the water tunnel before it occurs at the top of the test section.

Because the minimum pressure coefficient at the bottom surface is very close to zero, hydrostatic pressure will prevent cavitation from initiating

at the bottom surface for all three cases. When the top surface is flat, cavitation will initiate at the test section for any test section velocity. For the other two cases, cavitation may start near the contraction entrance if the test section velocity is below a certain magnitude. Some parameters related to the cavitation characteristics are listed in Table 3.

TABLE 3. Cavitation Characteristics of Three Alternative Contractions

Alternatives	z_o (m)	C_p (max)	U_{max} (m/s)
Nonsymmetrical	0	0.92	0
Intermediate	1.315	0.94	5.24
Symmetrical	2.63	0.95	7.37

Symbols in Table 3 are defined as follows:

z_o: Vertical distance between the top of contraction entrance and the top of contraction exit.

$(C_p)_{max}$: Pressure coefficient at the top of contraction entrance.

U_{max}: The critical test section velocity below which cavitation will initiate near the contraction entrance.

Based on the cavitation characteristics, we recommend the nonsymmetrical test section with flat top. We also recommend that the contraction be 8.7 meters long using fifth-order polynomials with the inflexion point at 5.22 meters from the exit. The equation for the recommended side wall and the bottom profiles are given below.

$$y = y_A + y_B \left[6\left(1 - \frac{x}{L}\right)^3 - 7\left(1 - \frac{x}{L}\right)^4 + 2\left(1 - \frac{x}{L}\right)^5 \right] \quad (5)$$

$$z = z_A + z_B \left[6\left(1 - \frac{x}{L}\right)^3 - 7\left(1 - \frac{x}{L}\right)^4 + 2\left(1 - \frac{x}{L}\right)^5 \right] \quad (6)$$

where x = longitudinal distance (m) measured from the contraction entrance,

y = lateral distance (m) measured from the plane of symmetry,

z = vertical distance (m) measured from the top surface,

$L = 8.7$ m, $y_A = 1.400$ m, $y_B = 0.715$ m, $z_A = 1.60$ m, $z_B = 2.630$ m

B. Turning Vanes

1. Profiles

Three types of turning vane profiles, (1) NACA(20)315, (2) K&R (III,IV), and (3) K&R (I,II), were considered for the first elbow located at the downstream end of the diffuser. The first profile is based on the NACA four digit airfoil series with a 20 percent camber. The two K&R profiles are based on circular arcs and have different thickness ratios. The K&R (III,IV) and K&R (I,II) profiles are shown in Figs. 13 and 14, respectively. The performance of the NACA(20)315 profile was previously analyzed and selected for the second elbow of the Large Cavitation Channel of DTNSRDC. The geometrical data of the K&R vanes were furnished by HSVA. Twelve vanes were used for all three cases. Both the inner and outer corners of the elbow were rounded with circular arcs whose radii were not changed for all three cases.

Somewhat different chord lengths as listed in Table 4 were selected more or less arbitrarily to fit the wall geometry. Because of the difference in the chord length used, a fair and precise comparison between the three cases analyzed may not be possible. In retrospect, it might be better to fix the chord length and adjust the radii of the elbow walls.

Table 4, Chord Lengths Used for Analysis

Vane Profile	Chord, mm
NACA(20)315	600
K and R (III,IV)	678
K and R (I,II)	695.5

2. Turning Angle

Typical velocity vector fields computed for three types of turning vanes, assuming uniform inflow velocity distribution, are shown in Figs. 15, 16, and 17. One of the most important performance criteria, the uniformity of the exit flow, was studied in detail for all three turning vane profiles. The predicted exit velocity distributions, including magnitude and direction, for three types of vanes each placed according to the design are shown in Figs. 18, 19, and 20. The quality of exit velocity distribution is indicated by two parameters. The uniformity parameter, Q_{D1}/Q_{D2}, is defined as the ratio of the discharge in the outer half of the elbow (Q_{D1}) and the discharge in the inner half of the elbow (Q_{D2}). When this number is greater than one, there is more flow near the outer wall than near the inner wall. The flow angle is defined as the angle between the exit velocity vector and the negative y-axis. A positive flow angle indicates that the vanes underturn the flow by that amount. Thus, underturning is indicated by $Q_{D1}/Q_{D2} > 1$ and a positive flow angle.

All three cases described above indicate slight underturning of varied degrees by these vanes. K&R (I,II) has the least amount and K&R (III,IV) has the greatest amount of underturning. One way to correct underturning is to increase the angle of attack by rotating each vane in the clockwise direction. The sensitivity of vane rotations to exit flow characteristics was tested. The exit velocity distribution for NACA(20)315 vanes rotated 1 degree, K&R (III,IV) vanes rotated 1.5 degrees, and K&R (I,II) vanes rotated 0.5 degrees; these are plotted in Figs. 21, 22, and 23, respectively. The estimated amount of vane rotation needed to achieve perfect turning is listed in Table 5.

Table 5. Vane rotation required for perfect flow turning

Vane Type	Vane rotation required (degrees)
NACA(20)315	1.0
K&R (III,IV)	2.0
K&R (I,II)	0.5

3. Pressure Distribution

The pressure distribution on each guide vane was calculated and studied. The peak negative pressure near the leading edge of the vane must be small to prevent cavitation. The adverse pressure gradient on the suction side should not cause boundary layer separation. Because there are many vanes, each with very small nose radius of curvature, a very large computational effort is required to compute the total flow field. This is particularly true if at the same time the pressure peaks near the leading edge are resolved accurately. There are two peaks, a stagnation point and a point of minimum pressure located very close to each other near the leading edge. Extremely small grids are needed to resolve the two peaks so closely located.

Fortunately, the resolution of the pressure distribution near the leading edge does not affect the accuracy of the results for exit velocity distribution nor the pressure distribution on each guide vane excluding a small area around the leading edge. For this reason, most runs were made with modest size grid systems having 6,400 grids. To adequately resolve the pressure peaks, each grid near the nose must be subdivided into 100 grids or more.

The pressure distribution on the inner vane, the center vane, and the outer vane for NACA(20)315 vanes at normal position computed with the coarse grid (6400 grids) system are plotted in Figs. 24, 25, and 26, respectively. The triangular symbols shown on these figures are the values obtained by the infinite cascade theory for NACA(21)315 foil designed to turn the flow ninety degrees. A similar set of graphs for K&R (III,IV) are shown in Figs. 27, 28, and 29. The cascade results were

included here only for a rough comparison. Exact comparison is not possible because there are slight differences in camber and the space-chord ratio between the two cases. The corresponding graphs for K&R (I,II) are shown in Figs. 30, 31, 32. In the above nine figures, the pressure coefficient C_p is defined as follows:

$$C_p = \frac{P - P_o}{\frac{1}{2} \rho U_o^2} \tag{7}$$

in which P_o and U_o are the average pressure and the average velocity at the exit section of the elbow.

The peak negative pressure on the K&R (III,IV) vane is most sensitive to the angle of attack change because it has the smallest radius of curvature. The pressure distribution on the three K&R (III,IV) vanes in a 1.5 degree overturned position are plotted in Figs. 33, 34, and 35. In Fig. 35, for an example, the positive $C_p = 1.0$ for the stagnation point is considerably underpredicted. On the other hand, the peak negative pressure is apparently somewhat overpredicted.

An effort was also made to resolve the peak pressure more accurately by using a nested grid system. A nested grid system is obtained by subdividing some of the original coarse grids near the leading edge into a number of smaller grids. A proper interpolation algorithm for the boundary between the fine grid zone and the coarse grid zone is used to pass the information between zones. Figure 36 shows the pressure distribution on the center vane of the K&R (III,IV) vane set at 1.5 degrees overturning position calculated by a nested grid system. In this grid system, each coarse grid near the nose was divided into 25 fine grids. The linear dimension of the smallest grid is about 0.7 times the radius of curvature of the nose. Although the resolution is still not perfect, significant improvement over the previous results is made evident by the sharp positive peak of magnitude a little less than one.

A finer nested grid system, a coarse grid divided into 100 fine grids, was also constructed and used for the center vane of K&R (III,IV) vane set at 1.5 degrees overturning position. In this case the size of the smallest grid is about 1/3 of the radius of curvature of the nose. Figure 37 shows that the stagnation pressure and the peak minimum pressure are fairly well resolved. There is some numerical instability, caused by the sudden change in grid size, near the boundary between the fine and coarse grid zones. The velocity vector field near the nose of the center vane is plotted in Fig. 38. This figure shows that the stagnation point is almost at the nose. It is interesting to note that the flow around the nose is very much like the flow around the front half of a circular cylinder resulting in two points of peak negative pressure, one on each side of the stagnation point. This is an advantageous characteristic with regard to the leading edge cavitation problem.

4. Boundary Layer Separation

The possibility of boundary layer separation was evaluated using the Stratford's separation criteria. Boundary layer separation is likely to occur if the Stratford number as defined below is equal to or greater than zero.

$$St = C_p \left(x \frac{\partial C_p}{\partial x} \right)^{1/2} - \alpha (10^6 Re)^{1/10} \qquad (8)$$

where

$$\alpha = \begin{cases} 0.39 \text{ if } \dfrac{d^2 C_p}{dx^2} > 0 \\ 0.35 \text{ if } \dfrac{d^2 C_p}{dx^2} < 0 \end{cases}$$

The Stratford number over the suction side of the six NACA (20)315 vanes near the inner wall of the elbow when they are placed at a normal position are plotted in Fig. 39. No separation is predicted because St is negative everywhere. Similar plots for K&R (III,IV) and K&R (I,II) vanes are shown in Figs. 40 and 41, respectively. Although no separation is indicated for any vanes, the K&R (I,II) vanes are closer to separation than other vanes.

5. Cavitation Susceptibility

The turning vanes of the elbow following the main diffuser of the upper leg are the most critical with regard to cavitation susceptibility. These vanes are exposed to higher velocities and lower pressures than the vanes in the other three elbows. Furthermore, the flow entering the first elbow is highly turbulent after exiting the diffuser.

The mean velocity distribution at the exit of the HYKAT diffuser is not known. However, the nonsymmetrical diffuser of the LCC is somewhat similar with a deflection angle of 5 degrees, although the area ratio of 3.12 was greater and the inlet and outlet cross-sections were both square rather than rectangular to square as in the HYKAT. Detailed measurements of both the mean and the fluctuating velocity profiles at the LCC diffuser exit showed considerable nonsymmetry. In that case, it has been found that the critical vanes for cavitation inception were near the center of the cascade.

By writing the energy equation between the diffuser inlet and exit, incorporating the estimated headloss coefficient for the diffuser, and using the ratio of maximum to average velocity as a parameter, it is possible to obtain an evaluation of the cavitation susceptibility of vanes as a function of the test section centerline cavitation number. The results of this calculation are shown in Fig. 42. The design test section σ_T was based on a test section velocity of 11.5 m/s, pressure of 0.05 bar,

and vapor pressure at 70°F. The cavitation number, σ_D, at the diffuser exit must exceed $-Cp_{min}$ of the turning vane for cavitation to be avoided. Thus, for a given velocity ratio, a, cavitation is unlikely for a vane with a $-Cp_{min}$ lying below the line. If a = 1.6 and for the design $\sigma_T = 0.157$, $-Cp_{min}$ should be less than 1.8. The pressure distributions of the vanes shown in Section III.B.3 have a Cp_{min} of about -1, indicating some margin against cavitation. However, the unsteadiness of the diffuser exit flow changes the angle of attack of the approach flow, and the margin is required. The three lines on Fig. 42 show the significance of the distortion of the mean velocity profile on cavitation susceptibility.

Unfortunately, it is not possible to make a definite choice between the three types of vanes with information available at this time. Although the K&R (I,II) vane appears to turn the flow most nearly equal to 90 degrees, it also turned out to be the one with the longest chord used for computation. NACA (20)315 foil is smallest but it turns the flow better than K&R (III,IV). Therefore, based on the flow turning characteristics above, either K&R (I,II) or NACA (20)315 is the best. NACA (20)315 foil performs best according to the flow separation criterion. K&R (III,IV) vanes appear to have the most uniform pressure distribution but, because it has the smallest nose radius, it is most sensitive to the angle of attack change. It is possible to improve the leading edge problem of K&R (III,IV) foil by increasing the nose radius. Furthermore, the inflow velocity distribution will be nonsymmetric because of the diffuser geometry, and an unknown amount of flow overturning will be needed. In view of these uncertainties, it is difficult to make a definite choice at this time.

IV. TURBULENCE MANAGEMENT SYSTEM

While considerable information on turbulence management exists for wind tunnels, information for water tunnels is sparse. Unfortunately, screens are the most commonly used device for turbulence control in wind tunnels, and they are not suitable for low noise water tunnels because of their tendency to "sing" in water flow. In many cases, turbulence control systems have been added to existing facilities for which the incoming turbulence level was a measured quantity. This is not known for the HYKAT, and any control system is based on assumptions as to its magnitude.

In our previous work on the Large Cavitation Channel (LCC), the problem was very similar. A design, using honeycombs, was proposed which was based on the theory presented by Lumley and McMahon [1967]. This theory has received some experimental verification in the 48 in. water tunnel at Pennsylvania State as reported by Robbins [1978]. The turbulence management system in that facility was able to reduce an incoming turbulence intensity of about 10 percent to about 0.1 percent in the test section after passing through a contraction with an area ratio 9 to 1.

The turbulence intensity in the test section is influenced by several factors. The honeycomb itself results in a reduction depending on the geometric characteristics of the honeycomb and the initial turbulence conditions. The length of the honeycomb cell must be sufficient to result in a fully developed turbulent flow at the cell exit. The turbulence generated by the honeycomb requires some distance to return to isotropy. This distance is estimated to be within 20 cell diameters of the downstream face of the honeycomb. Further reduction occurs over a decay length which is taken as the distance from the downstream face of the honeycomb to the contraction entrance plus one-third the length of the contraction. Turbulence reduction due to the contraction is based on the procedure suggested by Batchelor [1953], p. 74, for symmetrical contractions with circular cross sections. For a contraction ratio of four, the ratio of rms turbulence intensities in the test section to that at the entrance to the contraction is determined to be 0.36. It is not known how accurate this procedure is for a nonsymmetrical contraction with rectangular cross sections. Combining these effects, the rms turbulence intensity in the test section is determined by

$$u/U = n \cdot c \cdot \left(\frac{I}{L'}\right)^{1/2}$$

where n = rms turbulence intensity downstream of honeycomb

c = rms turbulence intensity reduction in contraction

I = distance for return to isotropy

L' = decay distance

Design charts are presented by Lumley and McMahon [1967] to predict the turbulence reduction and local loss coefficients for the honeycomb. The method requires knowledge of the incoming turbulence length scale and a turbulent flow in the cell. If the local loss coefficient for the honeycomb, defined as the pressure drop divided by the dynamic pressure, is approxi-mately two and the length of the cell is made equal to the integral scale, then a large change or error in assumption for integral scale will not seriously degrade the performance of the turbulence management system. It will quickly be discovered that these conditions are difficult to meet for many operating conditions of interest. Therefore, the alternative of designing to exceed a target value in most cases must be accepted so that the worst case operation will be satisfactory.

As the integral length scale is not known, a value for computational purposes has been assumed which is equal to the expected spacing of the turning vanes in the elbow just upstream of the honeycomb. Assumptions also have to be made regarding the turbulence level downstream of the turning vanes. The minimum velocity in the test section was assumed to be 3 m/s as a worst case condition. The summary of input data is listed below:

Contraction ratio	4
Plenum length	3.49 m
Contraction length	8.7 m
Min. test section velocity	3 m/s
Incoming turbulence level	10%
Integral length scale	25 cm
Desired test section turbulence level	0.1%
Water temperature	20C

The results for several honeycomb geometries are given in Table 6.

TABLE 6

Cell Diameter	Cell Length	Loss Coefficient	n	I	L'	c	u/U
cm	cm	k	rms	cm	cm	rms	rms
0.3	15	2.6	0.019	6	624	0.36	0.00067
0.6	33	2.2	0.0185	12	606	0.36	0.00094
1.0	60	2.0	0.018	20	579	0.36	0.0012
1.0	80	2.7	0.015	20	559	0.36	0.0010
3.0	240	1.9	0.013	60	399	0.36	0.0018

The smallest cell diameter which would result in fully turbulent flow at the 3 m/s test section velocity is 0.3 cm. It can be seen that the target value of 0.1% can be achieved with a cell diameter of 0.6 cm, with a loss coefficient of 2.2. This result was based on a single honeycomb, and the possibility of better performance using two honeycombs was examined.

Using the same initial conditions of turbulence, i.e., 25 cm integral length scale and 10 percent turbulence level, a combination of two honeycombs in tandem was selected. The first honeycomb has a cell diameter of 2 cm and length of 40 cm, and the second honeycomb has a cell diameter of 1 cm and a length of 20 cm. From the design charts of Lumley and McMahon, the first honeycomb has a loss coefficient of 0.66 and a turbulence reduction factor of 0.235. Thus, the turbulence intensity at the upstream face of the second honeycomb is 0.0235. The two honeycombs are separated by the distance estimated to achieve isotropy (20 diameters or 40 cm). The integral scale of the turbulence impinging on the second honeycomb is now assumed to be 2 cm. Again from the charts, the loss coefficient is 0.85 and the turbulence reduction factor is 0.13, with a turbulence level at isotropy of 0.00306. Including the decay length and contraction reduction, the test section turbulence level is estimated to be 0.0002 for an incoming turbulence level upstream of the first honeycomb of 0.1. This provides for some margin of error in the prediction. The loss coefficient for the single honeycomb was about 2.2 and for the combination about 1.5. At the test section design velocity of 11.5 m/s, the turbulence level remains about the same and the local loss coefficient reduces to about 1.3.

It must be pointed out that little evidence exists that turbulent intensity levels of less than 0.001 can be achieved in a water tunnel test section due to sound and vibration generated in the tunnel power system. These can be readily transmitted through the water and steel of the flow circuit with little or no attention by the turbulence management system.

V. HEAD LOSS

A. General

Estimates have been made of the head loss for each component in the flow circuit. The elbows are numbered consecutively, starting with number one, following the diffuser in the upper leg of the tunnel. A local head loss coefficient, K_ℓ, has been defined based on the local average velocity, V_ℓ, as

$$h_\ell = K_\ell \frac{V_\ell^2}{2g}$$

It is customary to define a loss coefficient in terms of the test section velocity, V_T, or

$$h_\ell = K_T \frac{V_T^2}{2g} = K_\ell \frac{V_\ell^2}{2g}$$

or

$$K_T = K_\ell \left(\frac{V_\ell}{V_T} \right)^2 = K_\ell \left(\frac{A_T}{A_\ell} \right)^2$$

where A_T is the area of the test section and A_ℓ is the area of the particular component. A design test section velocity of 11.5 m/s was used.

B. Component Losses

1. Test Section

The head loss in the test section is calculated assuming an equivalent flat plate for the boundaries. With a test section length of 11 m, the length Reynolds number is about 1.3×10^8. Using a skin friction coefficient, C_f, of

$$C_f = \frac{0.455}{(\log_{10} \mathrm{Re})^{1.58}} = 0.0021$$

then, the head loss is

$$h_L = \frac{\Delta P}{\gamma} = \frac{C_f}{2} \frac{A_p}{\gamma} \delta \frac{V_T^2}{A_T} = C_f \frac{A_p}{A_T} \frac{V_T^2}{2g} = K_T \frac{V_T^2}{2g}$$

where A_p is the wetted surface area and A_T is the cross-sectional area of the test section. Since $A_p = 96.8\ m^2$ and $A_T = 4.48\ m^2$, $K_T = 0.0454$.

2. Diffuser

The nonsymmetry and the shape change of the diffuser makes it somewhat difficult to estimate the loss coefficient. The diffuser can be considered to consist of two parts: a transition of constant width with a curved bottom surface and the straight sided diffuser itself. The bottom transition is similar to that used in the LCC design, which was given by a fourth order equation. The length and offset were established to provide a continuous slope at the junction of the curved and straight section. With the dimensions indicated in the preliminary design shown in Fig. 1, a discontinuity exists at the juncture using a fourth order equation. A cubic equation provides a better match. For purposes of head loss estimates, the particular shape selected may not be significant.

As the ratio of the exit to inlet area of the transition is only slightly greater than one, the head loss in this section is calculated, assuming that it is just an extension of the test section. With $C_f \sim 0.0021$ and a 3 m length, the loss coefficient is about 0.0124.

The head loss in the diffuser itself is associated with an expansion loss and a friction loss. The expansion loss coefficient is a function of geometry, i.e. area ratio, length, and included angle, whereas the friction loss may be a function of the Reynolds number through the selection of the friction coefficient.

The main diffuser also has a change in shape being rectangular at the entrance and square at the exit, as compared to the LCC main diffuser which was essentially square-to-square with a larger area ratio. Some information for a pyramidal diffuser has been presented in I'delchik [1986] for the case with different angles for the side and bottom walls. These results were used to calculate the loss coefficients for the HYKAT diffuser. It has been assumed that the flow enters the diffuser symmetrically, and that the total included angle of the diffuser is 5.6 degrees. In the horizontal plane, the total included angle is 1.6 degrees. With these values and an area ratio of 2.16, the expansion loss coefficient is about 0.048. The friction loss component, assuming a friction coefficient of 0.0095, is about 0.042 so that the total local head loss coefficient is 0.090. In terms of the test section velocity, the coefficient is reduced by the square of the ratio of the test section to entrance area and is about 0.080. The total loss for the transition-diffuser is therefore about 0.092. Increasing the length of the diffuser reduces the included angles, although modest increases in length do not appreciably change the head loss estimates for the combination of the transition and diffuser.

3. Elbows

The profile to be used for the turning vanes in the elbows has not been fixed at this time. However, it appears that the space to chord ratio will be approximately one-half. This is the value used for the 4-digit series vanes in the elbows for the LCC, and a local loss coefficient of 0.14 was assumed for those elbows.

For vanes made up of circular arcs, the same loss coefficient has been assumed. This is somewhat substantiated by wind tunnel experiments as reported by Gelder et al. [1986]. It should be pointed out that the flow from the diffuser can have a significant influence on the performance of the vanes and the head loss in the first elbow. The two components should be considered together, as would be done in physical model tests.

4. Square to Circular Transition

The area ratio of this transition is 1.16. The charts for diffusers do not give values for a loss coefficient at such low area ratios and lengths. However, considering the transition as a straight pipe with a mean diameter of 3.76 m, length of 4 m, and a friction factor of 0.0095, the local loss coefficient is 0.01.

5. Acoustic Grids

These grids are the same as proposed for the LCC, and consist of 25 mm thick parallel bars spaced on 152 mm centers with a length of 457 mm. Another unit of bars is placed below this unit but with the bars running perpendicular to it. Such a configuration was suggested to reduce blockage of the flow. The loss coefficients were calculated based on resistance of flat plates and a diffuser action of the downstream end of the bars.

6. Straight Pipe Upstream of Pump

Assuming a length of straight pipe of 12.5 m and diameter of 3.9 m, the friction factor for a commercial steel pipe is about 0.0095. This results in a local loss coefficient of 0.030.

7. Contraction Upstream of Pump

The area ratio of this contraction with diameters of 3.9 and 3.775 m is about 1.07. Therefore, the head loss is calculated on the basis of a 1 m length of straight pipe with a mean diameter of 3.84 m and a friction factor of 0.005. The local loss coefficient is thus 0.0025.

8. Lower Leg Diffuser

The conical diffuser has a length of 8.3 m and a diameter change from 3.775 to 4.78 m. This results in an area ratio of 1.6. From the charts, a value of about 0.06 is found for the local loss coefficient.

9. Straight Pipe - Lower Leg

A friction factor of 0.009 was assumed. Thus for a 7.2 m length of 4.78 m diameter pipe, the local loss coefficient is 0.014.

10. Transition

With an inlet area of 17.95 m^2 and an exit area of 17.89 m^2, it is assumed that the transition can be considered a straight pipe of 6.5 m length. Using a friction factor of 0.009, the local loss coefficient is about 0.012.

11. Upcomer

Assuming the length of the 4.23 m square upcomer is about 4.5 m, with a friction factor of 0.009, the local loss coefficient is 0.0096.

12. Acoustic Grid

The acoustic grid has the same configuration as in the downcomer. The velocity is slightly lower, which results in a local loss coefficient of about 0.12.

13. Turbulence Management System

The two honeycombs placed in tandem with a combined loss coefficient of 1.5 are proposed as discussed in Section III.

14. Contraction

The loss coefficient of the contraction has been estimated to be 0.02. This is difficult to estimate accurately, but fortunately the error associated with this estimate is very small.

The values of component head losses are tabulated in Table 7. It can be seen that the largest losses occur in the components of the upper leg, i.e. the turbulent management system, test section, and diffuser. With the head loss of about 2.42 m, at the design test section velocity of 11.5 m/s, the power to be delivered by the pump is about 1220 KW. For an assumed pump efficiency of 80 percent, the power delivered to the shaft is 1527 KW. Eliminating the acoustic grids and the honeycomb, the power requirement at the shaft reduced to 940 KW.

TABLE 7. Estimate of Component Head Loss

Component	Pertinent Local $A(m^2)$	Pertinent Local $V(m/s)$	Local K_ℓ	$H_\ell(m)$
Test section (1.6mx2.8m)	4.48	11.5	0.046	.310
Main Diffuser	4.48	11.5	0.092	.620
1st Elbow	10.31	5.00	0.14	.178
Acoustic Grid	10.31	5.00	0.11	.28
Downcomer Transition	10.31	5.00	0.01	.013
2nd Elbow	11.89	4.31	0.14	.132
Leg Upstream of Pump	11.89	4.31	0.031	.028
Contraction Downstream of Pump	11.89	4.31	0.003	.003
Diffuser Downstream of Pump	11.15	4.60	0.06	.065
Large Dia. Leg Downstream of Pump	17.93	2.87	0.014	.006
Contraction/Transition	17.93	2.87	0.0122	.005
3rd Elbow	17.84	2.88	0.14	.059
Upcomer	17.84	2.88	0.01	.004
Acoustic grid	17.84	2.88	0.12	.101
4th Elbow	17.84	2.88	0.14	.059
Honeycomb	17.84	2.88	1.6	.549
4:1 Contraction	17.84	2.88	0.02	.008
			ΣH_ℓ =	2.42 m

This corresponds to a system K_T based on a test section velocity of 11.5 m/s of K_T = 0.359.

VI. SQUARE SECOND ELBOW

In the preliminary design configuration of the KYKAT the second elbow is circular in cross section. During the development of the LCC, consideration was given to the possible use of a square elbow instead. It was anticipated that the square elbow may result in a better turning of the flow since the turning vanes would be of the same length. Some advantages in construction and fabrication were also noted, as the acoustic grid in the revised square downcomer would be simplified. To evaluate the performance of a square elbow as compared to a round elbow, some tests were carried out in a wind tunnel facility and reported by Cary [1985].

The particular concern of the tests was to establish the velocity distribution at the intake to the pump. The quality of the inflow was determined by a parameter given by

$$QP = \left[\sum_{n=1}^{N} \frac{C_n^2}{n} \right]^{1/2}$$

where C_n is the amplitude of the nth harmonic of the velocity non-uniformity. A low value of QP was sought. The experimental measurements indicated very little difference in QP for the square or round second elbow. At that time, a square elbow was recommended but was not adapted due to time constraints and modifications required in the structural design.

In the LCC design, the pump was located some distance downstream of the second elbow to improve the flow quality at the pump intake. The length of straight connecting pipe used in the tests was about two pipe diameters. An extensive study was not conducted to optimize this length due to other constraints. This was of some concern, particularly with the square elbow, as the elbow was followed with a square to round shape transition. However, the length appeared to be sufficient to not significantly affect the quality parameter.

VII. DIFFUSER TRANSITION

As briefly mentioned in Section VB.2, the bottom curve of the transition between the test section and the diffuser itself was not defined in the preliminary concept of the HYKAT. For the LCC, the bottom curve was given by a fourth order polynomial. If a fourth order curve is used for a transition length of 3 m and deflection of 0.1 m as shown in Fig. 1, the tangent is not continuous at the conjunction of the transition and the diffuser. This discontinuity can be eliminated by increasing the length of the transition by about 1 m.

Another alternative is to use a cubic equation for the curve with the original length and deflection. In this case, the tangent is essentially continuous. It should be noted that the original length of the HYKAT has been increased by 2 m over the length shown in Fig. 1. The length of the contraction has been increased from 2.7 to 8.7 m, so that an additional meter remains. This could be added to the transition or the diffuser. It is suggested that the transition curve be represented by the cubic equation with a length of 3 m. The extra 1 m would then be added at the exit of the diffuser to provide additional approach length to the first elbow and perhaps some improvement of the flow quality at that location.

VIII. CONCLUSIONS

The following conclusions have been drawn from the results of the mathematical modeling:

1. Three configurations of a contraction with a profile given by a fifth-order polynomial were examined. Two lengths of the contraction were used, and the contraction ratio of four was held constant. By comparing cavitation characteristics, velocity uniformity, and boundary layer characteristics, the nonsymmetrical contraction with a flat top is recommended due to its superior cavitation resistance. The recommended contraction has a length of 8.7 m and inflection point located 5.22 m from the exit.

2. Three vane profiles were evaluated; one based on the NACA four digit series airfoil section, and two based on circular arc sections. Criteria used for evaluation were turning action and pressure distribution for both uniform and nonuniform inflow velocity distribution. Based on flow turning characteristics, either the K&R (I,II) or NACA (20)315 is best. The K&R (III,IV) profile has the most uniform pressure distribution but is most sensitive to change in angle of attack. Although no boundary layer separation was predicted, the greatest margin against separation was found for the NACA (20)315 profile. Cavitation susceptibility is dependent on the nonuniformity of the velocity profile at the exit of the main diffuser. Using an assumed distortion of the profile, the vanes have some margin against cavitation.

Additional studies are required to select the optimum turning vane geometry.

3. A turbulence management system was recommended using two honeycombs in tandem. The system was based on assumptions of the incoming turbulence intensity and the integral length scale.

4. Head loss computations were made for the complete flow circuit with the 1.6x2.8 m test section. At the design test section velocity of 11.5 m/s, the power requirement at the shaft for an assumed pump efficiency of 80 percent is about 1500 kW. Eliminating the two acoustic grids, the power requirement is reduced to about 1280 kW.

5. It is recommended that the second elbow (upstream of the pump) be of square cross section. The transition from square to round will then occur downstream of the second elbow.

REFERENCES

Batchelor, G. K., Homogeneous Turbulence, Cambridge University Press, 1953.

Cary, Charles M., "BBN Phase A-2 (Extended) Experiments in Support of LCC Turning Vane Design," Tech. Memo. No. 854, Bolt, Beranek, and Newman, Inc., January 1985.

Gelder, T. F., Moore, R. D., Sanz, J. M. and McFarland, E. R., "Wind Tunnel Turning Vanes of Modern Design," AIAA-86-0044, paper presented at AIAA 24th Aerospace Science Meeting, January 6-9, 1986, Reno, Nevada.

I'delchik, I. E., Handbook of Hydraulic Resistance, 2nd Edition, Hemisphere Publishing Corporation, 1986.

Lumley, J. L. and McMahon, J. F., "Reducing Water Tunnel Turbulence by Means of a Honeycomb," Trans. ASME, Journal of Basic Engineering, Vol. 89, Dec 1967, pp. 764-770.

Robbins, Basil, "Water Tunnel Turbulence Measurements Behind a Honeycomb," Journal of Hydronautics, Vol. 12, No. 3, July 1978, pp. 122-128.

LIST OF FIGURES

Figure No.

Figure No.

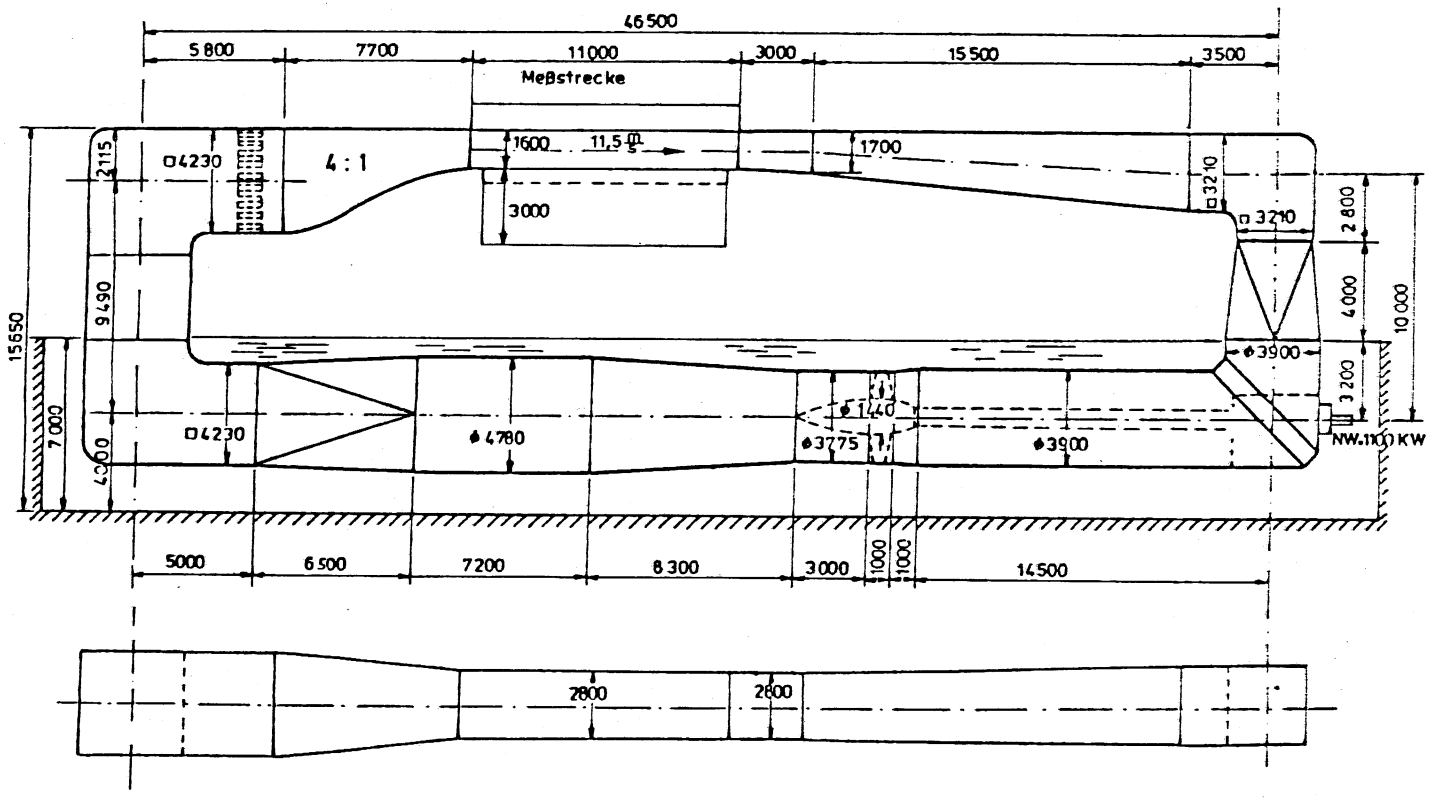

Figure 1. First design of HYKAT.

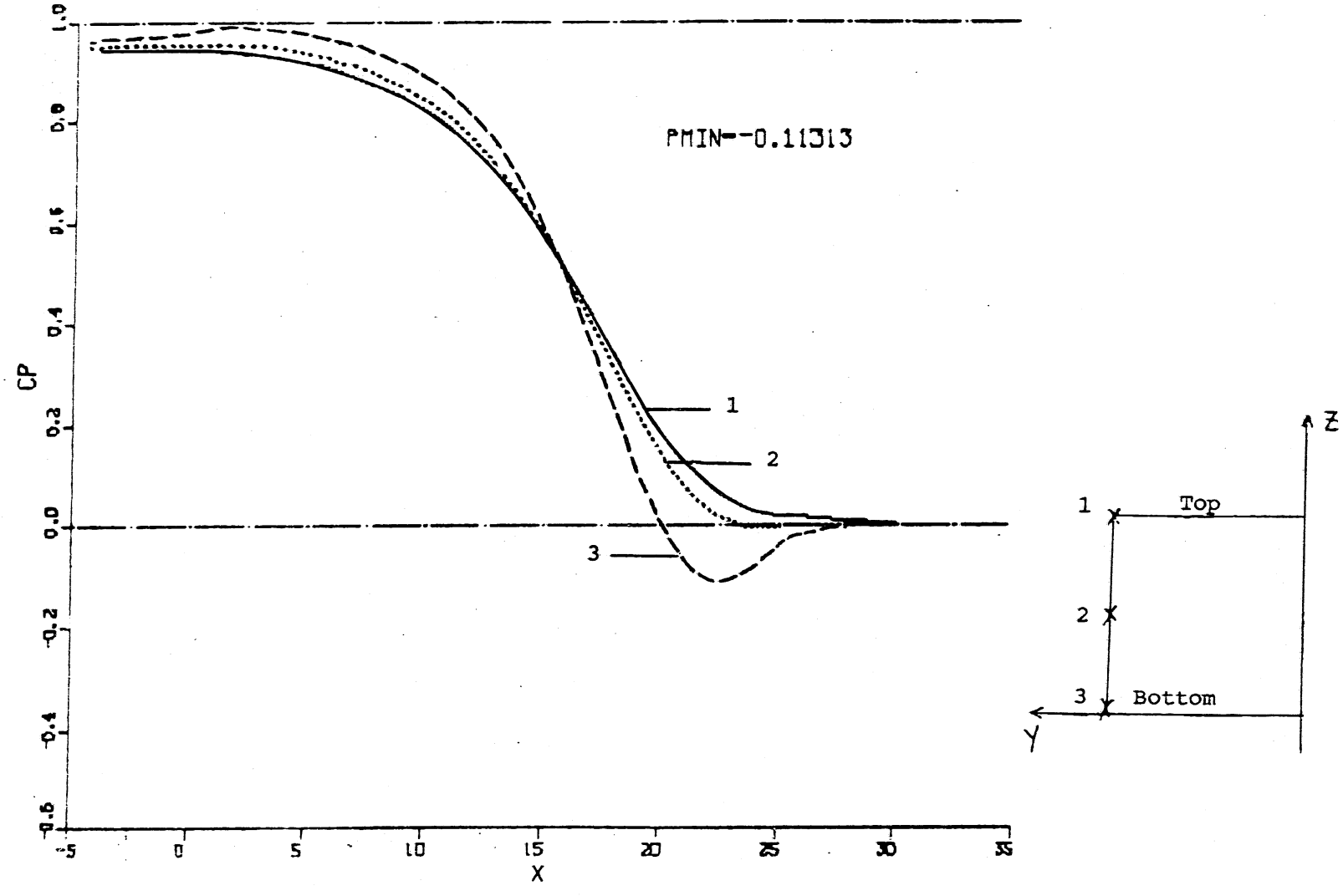

Figure 2. Pressure distributions along three streamlines on a sidewall--first design.

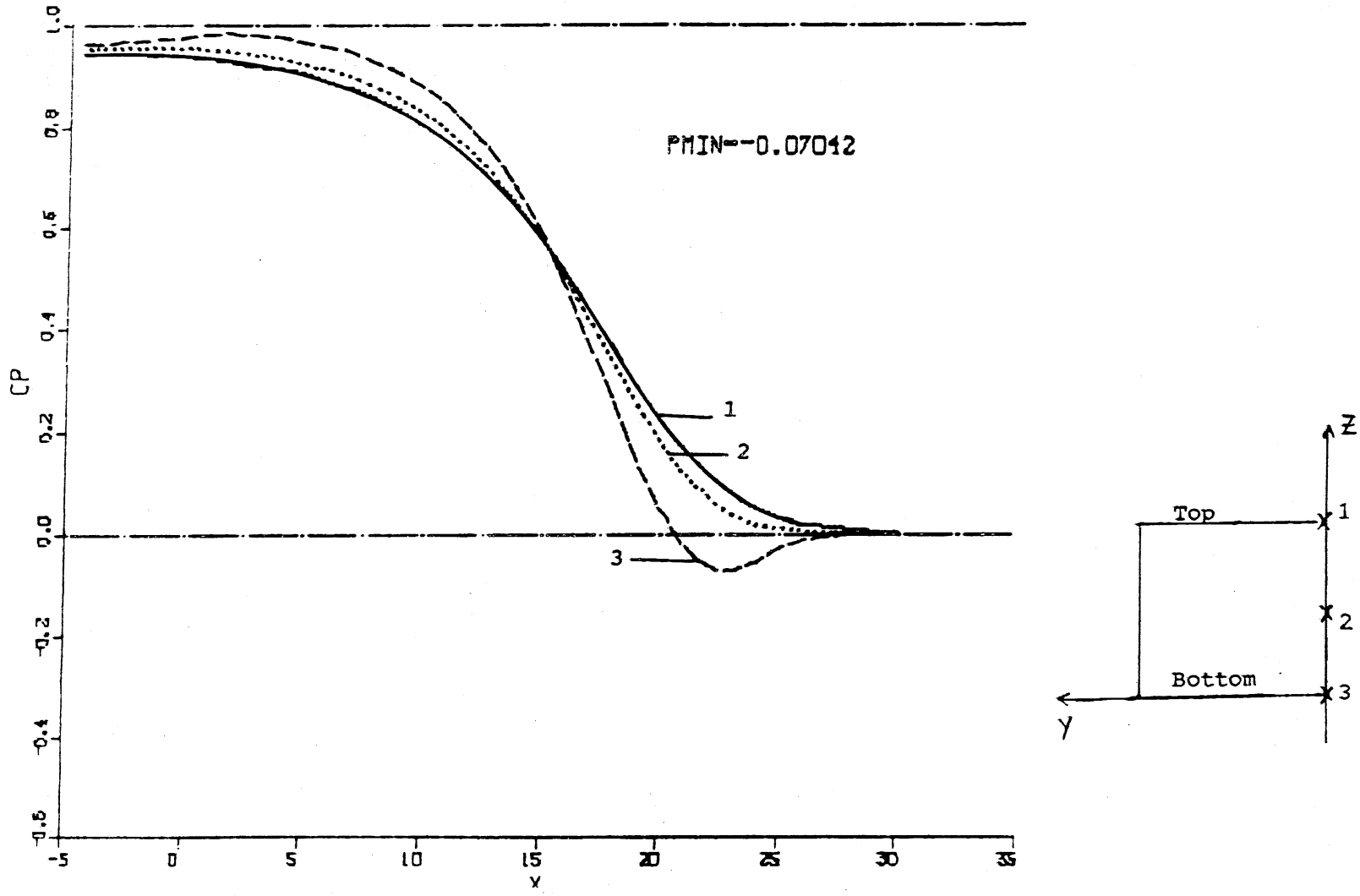

Figure 3. Pressure distribution along three streamlines on the plant of symmetry--first design.

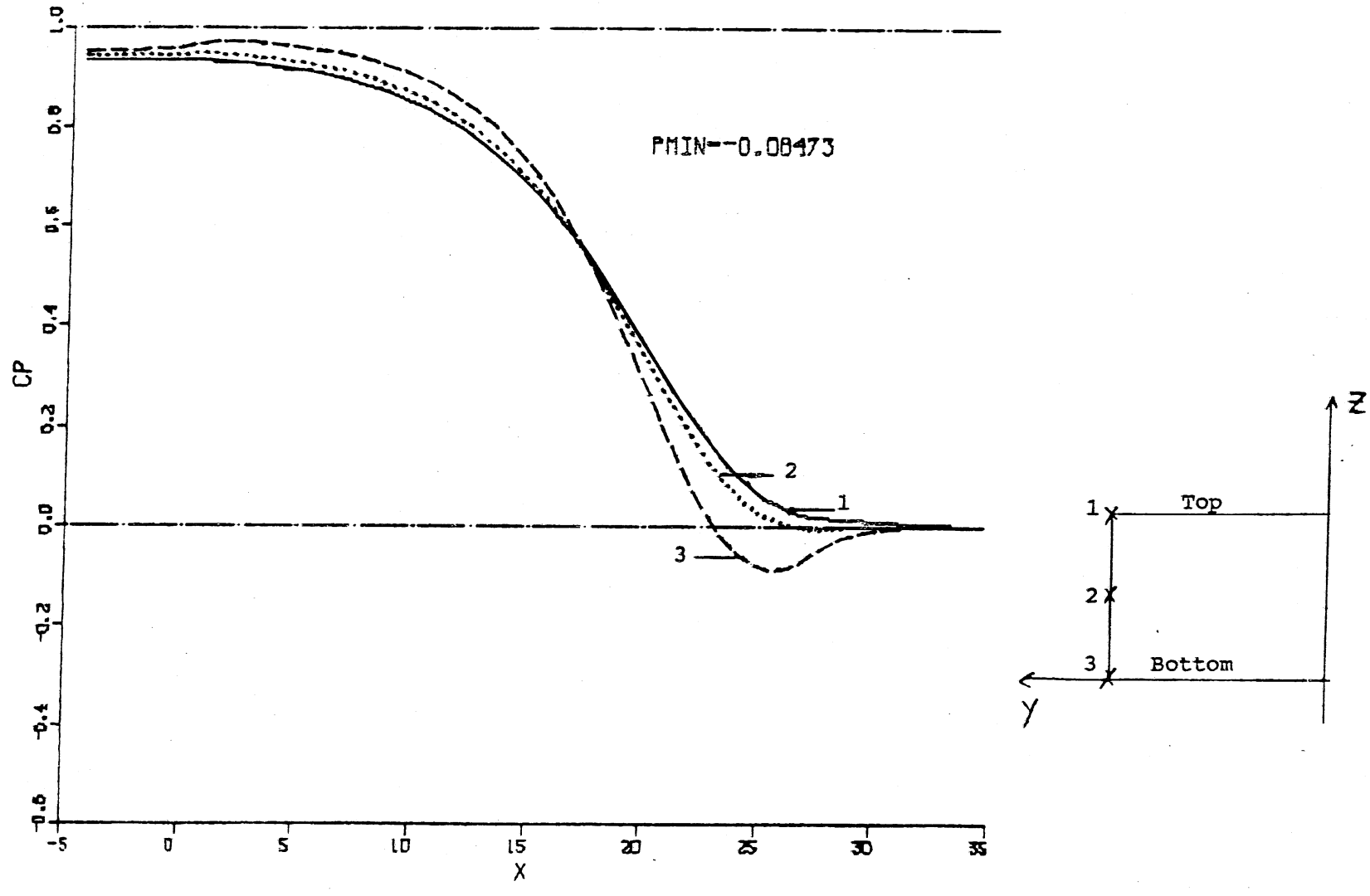

Figure 4. Pressure distribution along three streamlines on a sidewall--contraction 1 m longer.

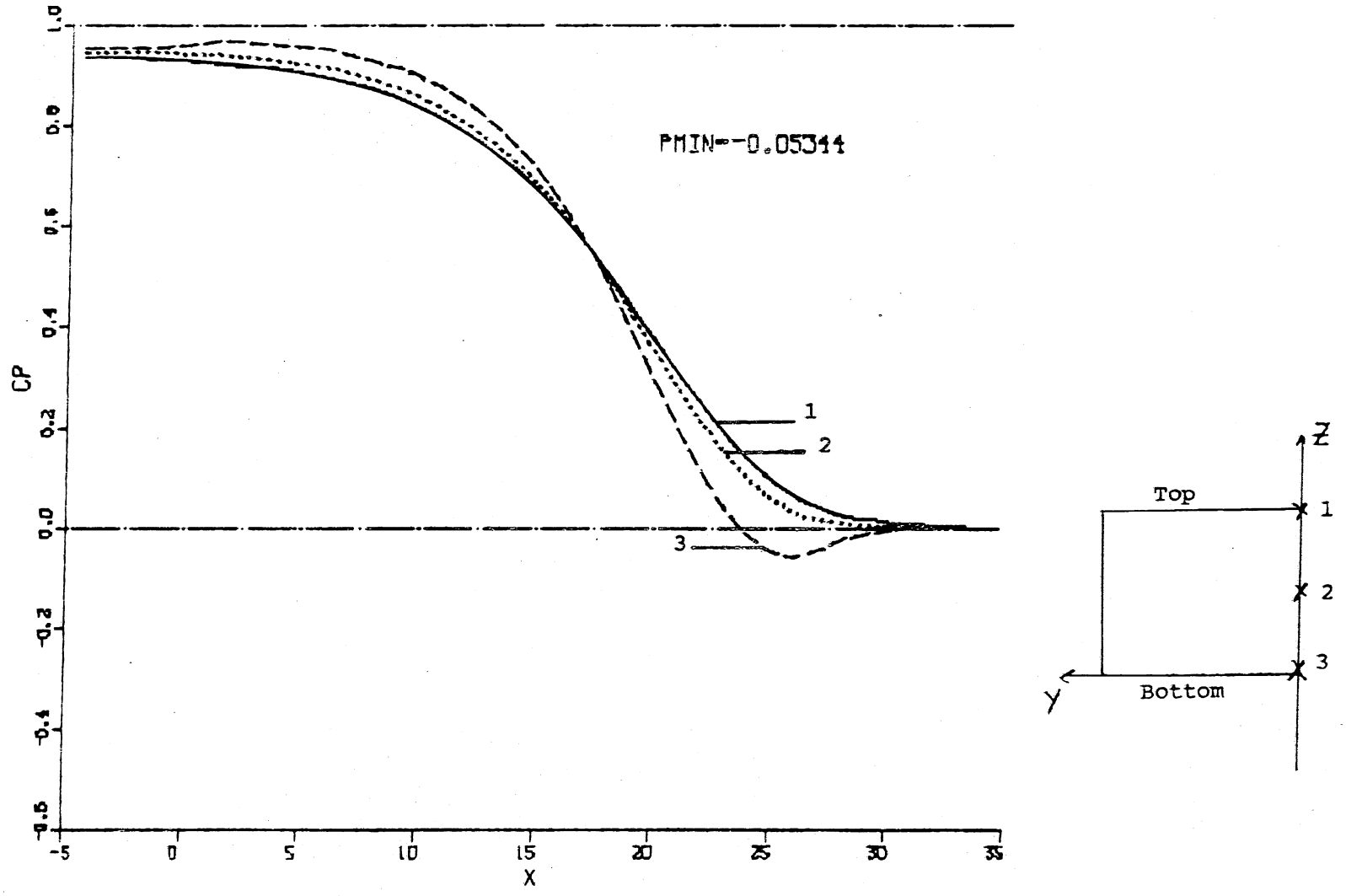

Figure 5. Pressure distribution along three streamlines on the plane of symmetry--contraction 1 m longer.

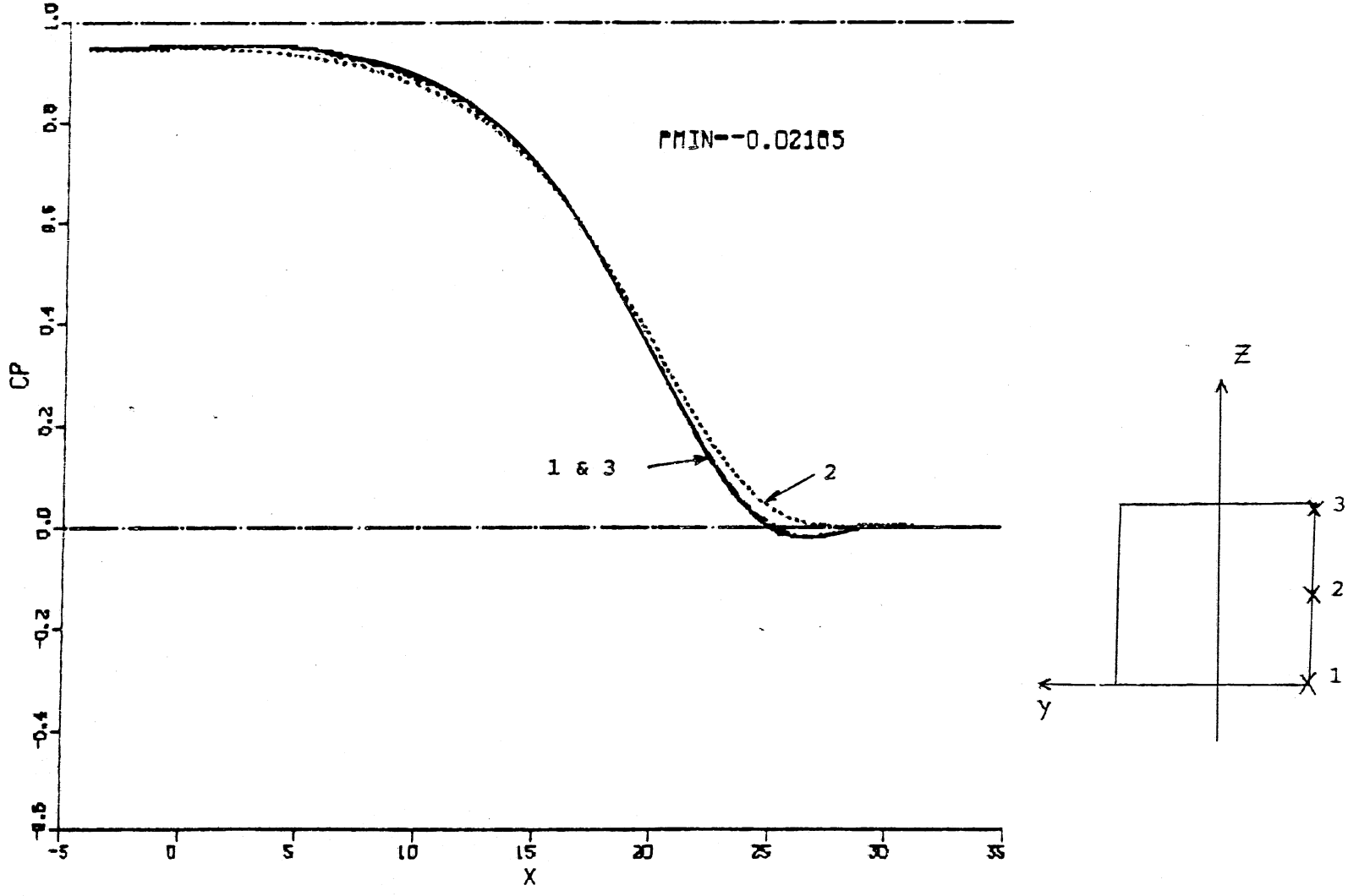

Figure 6. Pressure distribution along three streamlines on a side wall--symmetrical and longer contraction.

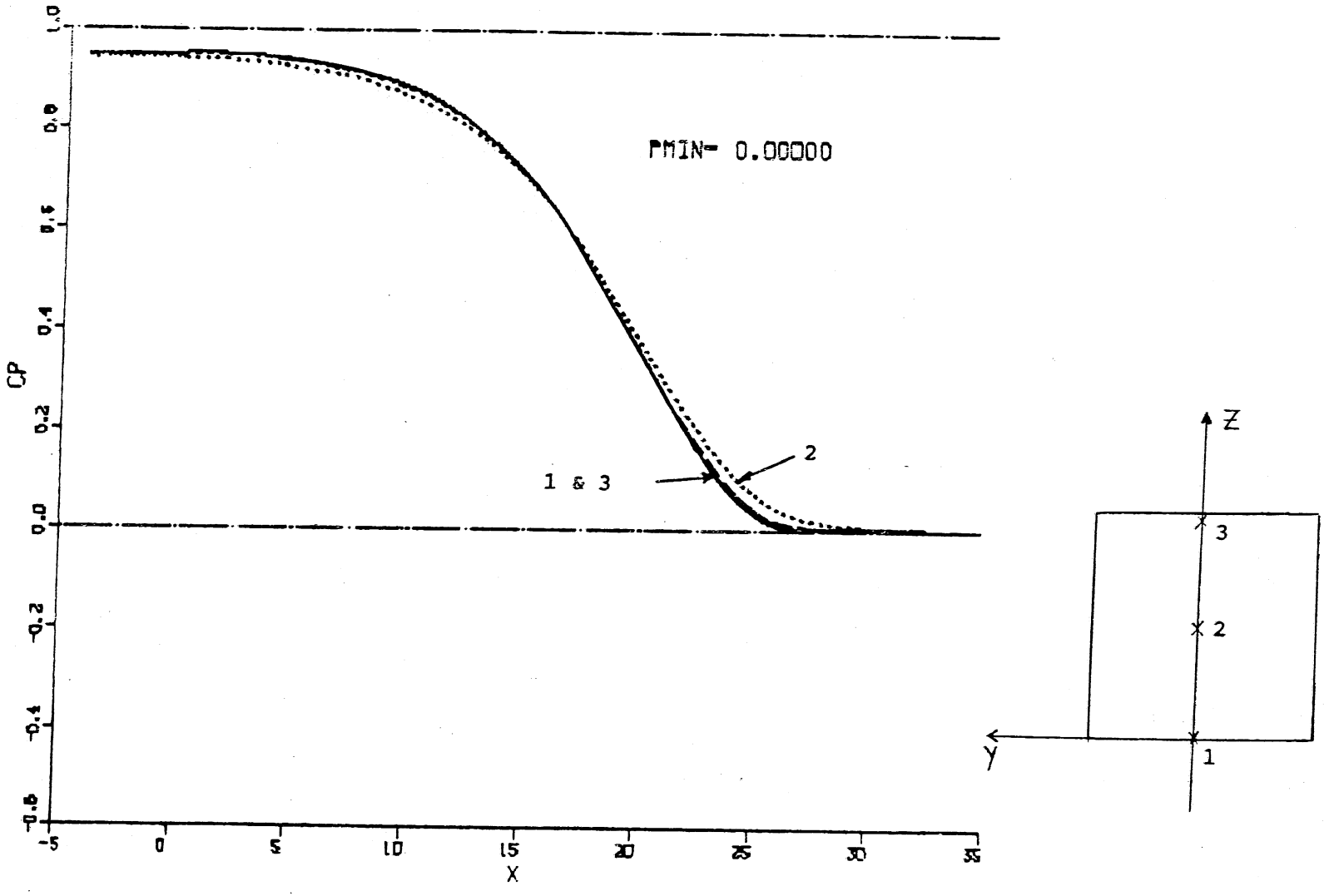

Figure 7. Pressure distribution along three streamlines on a vertical plane of symmetry--symmetrical and longer contraction.

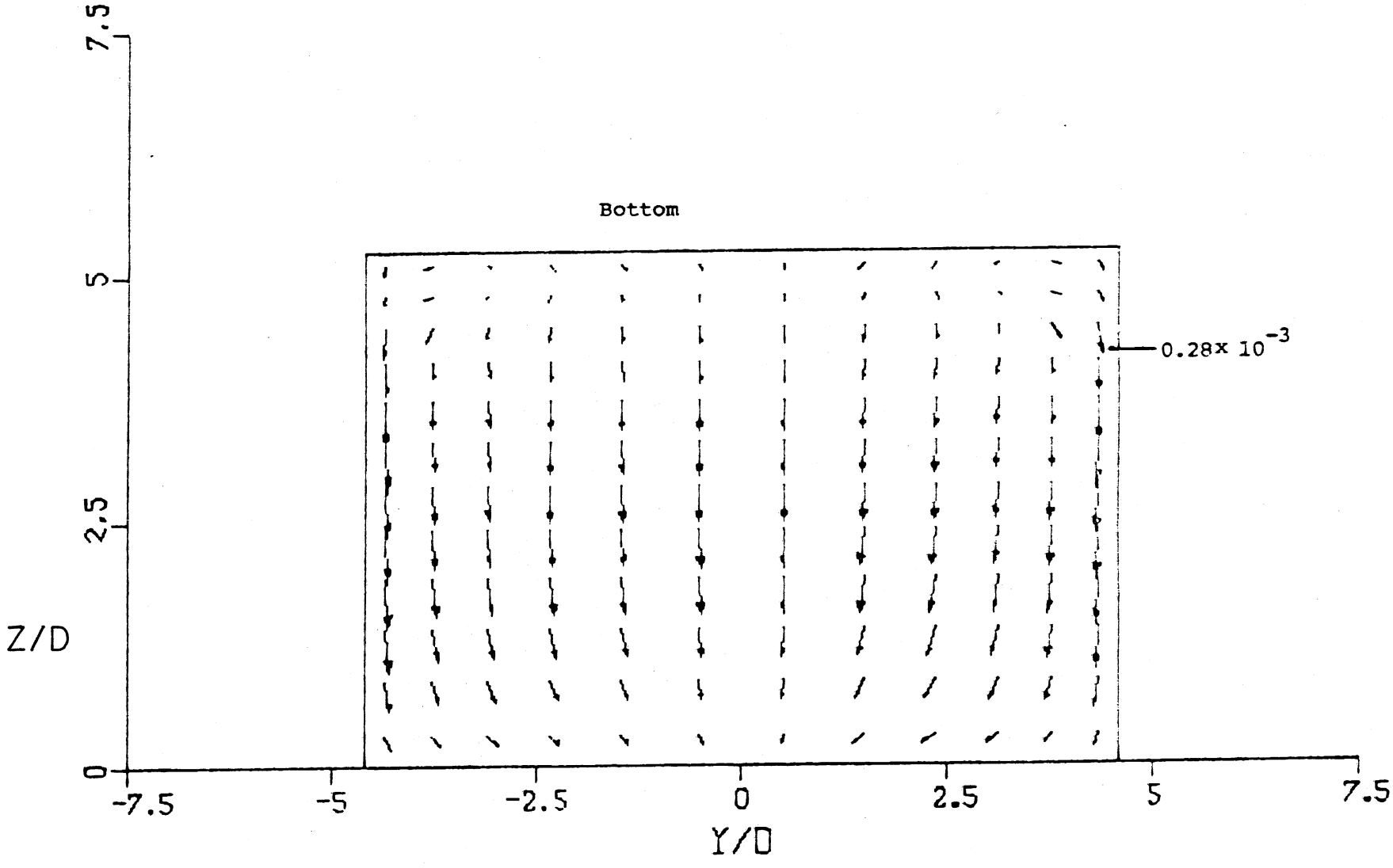

Figure 8. Secondary currents at contraction exit--nonsymmetrical longer contraction.

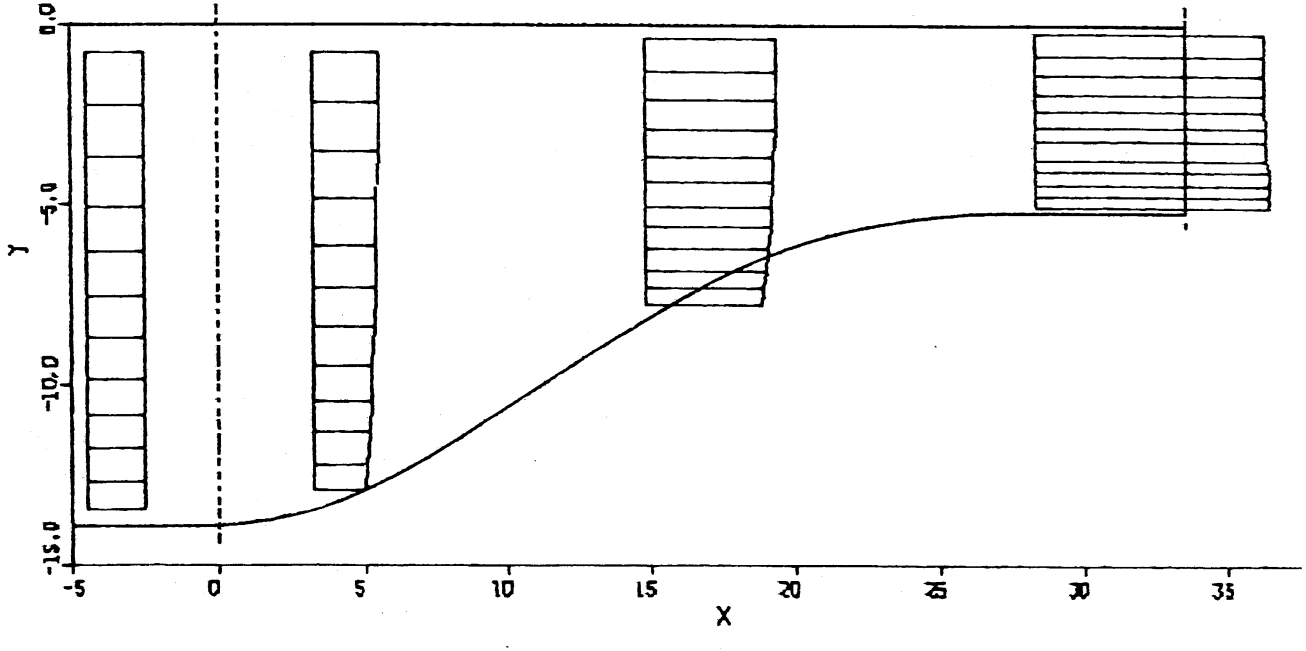

Figure 9. Velocity distribution on the plane of symmetry--nonsymmetrical contraction, uniform inflow.

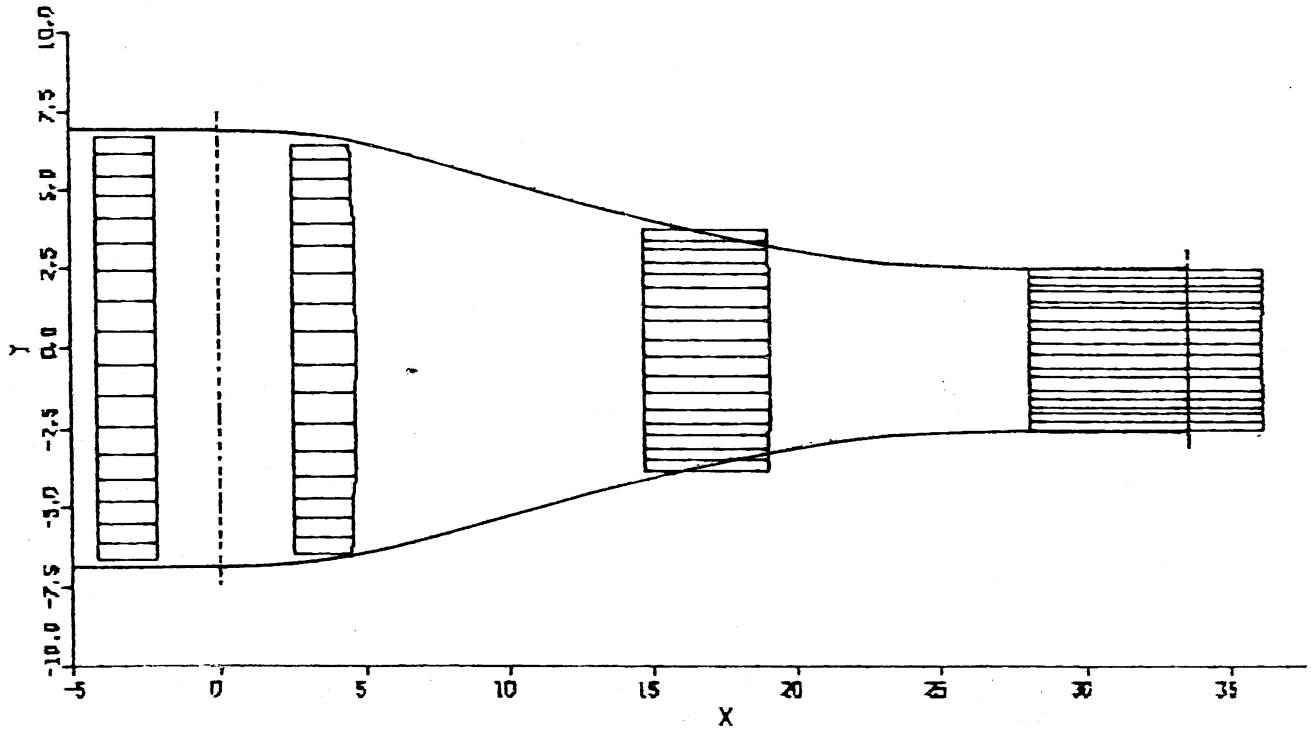

Figure 10. Velocity distribution on the plane of symmetry--symmetrical contraction, uniform inflow.

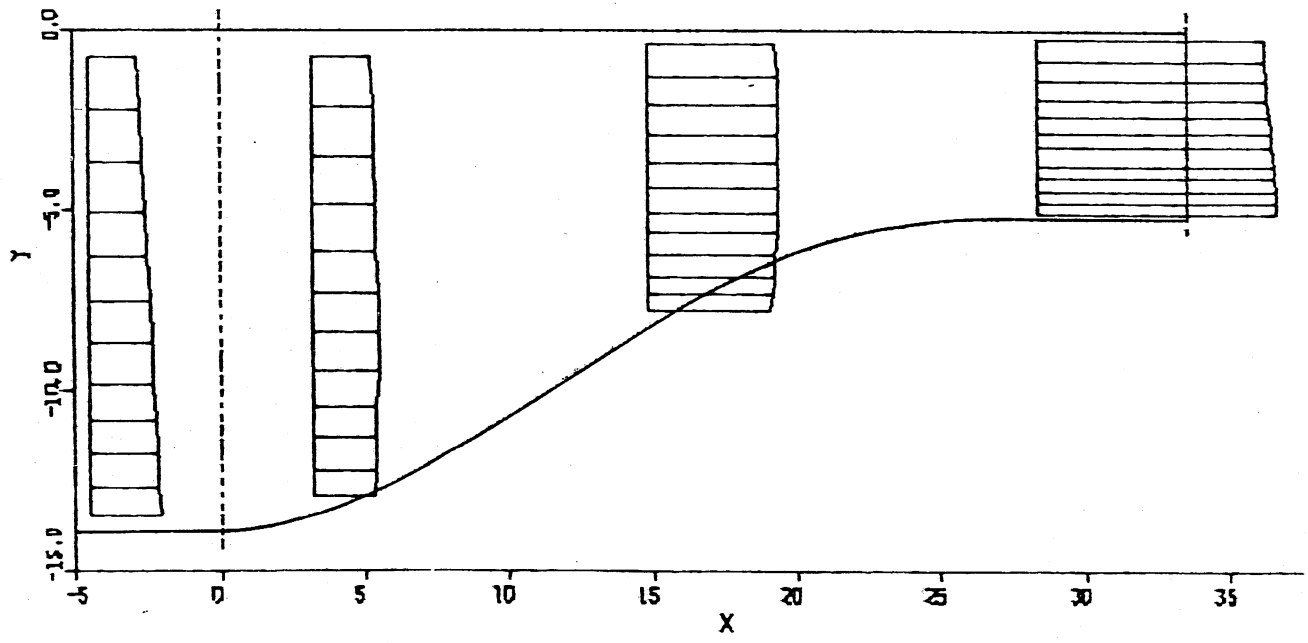

Figure 11. Velocity distribution on the vertical plane of symmetry--nonsymmetrical contraction, nonuniform inflow.

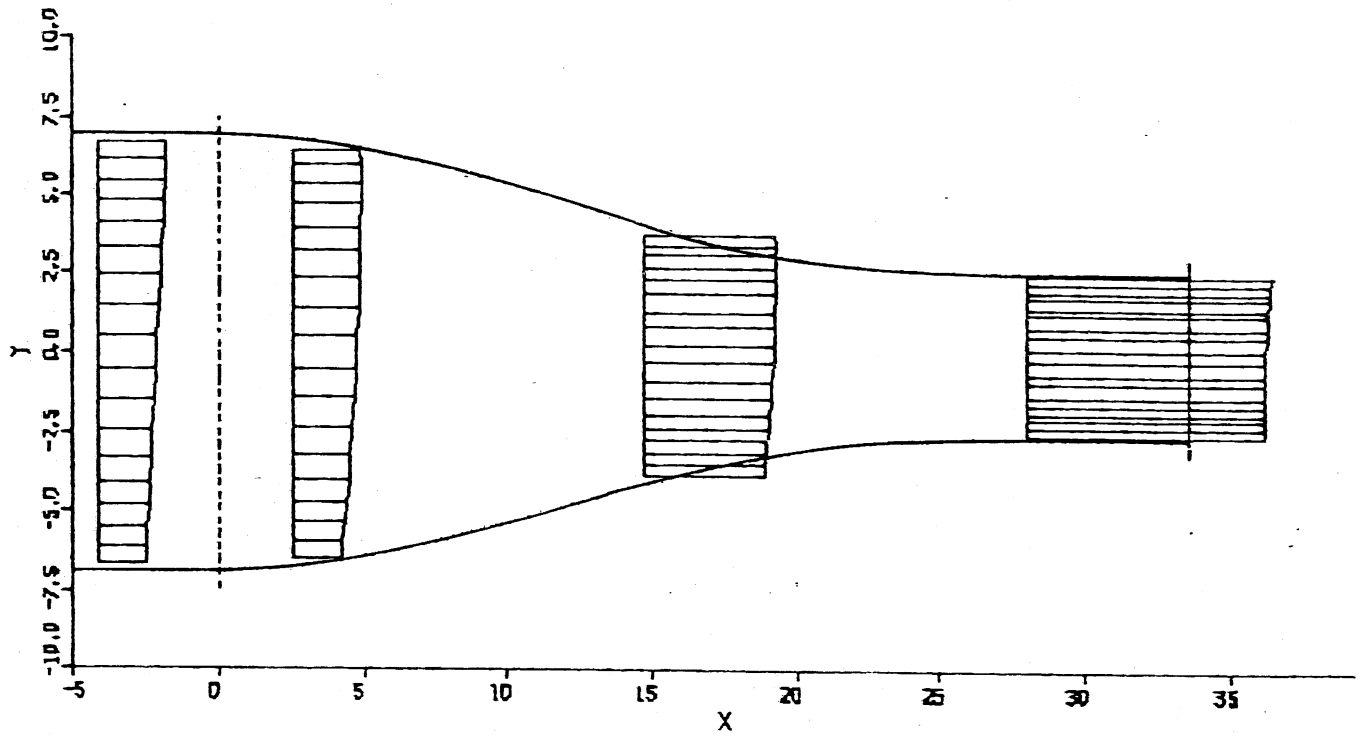

Figure 12. Velocity distribution on the vertical plane of symmetry--symmetrical contraction, nonuniform inflow.

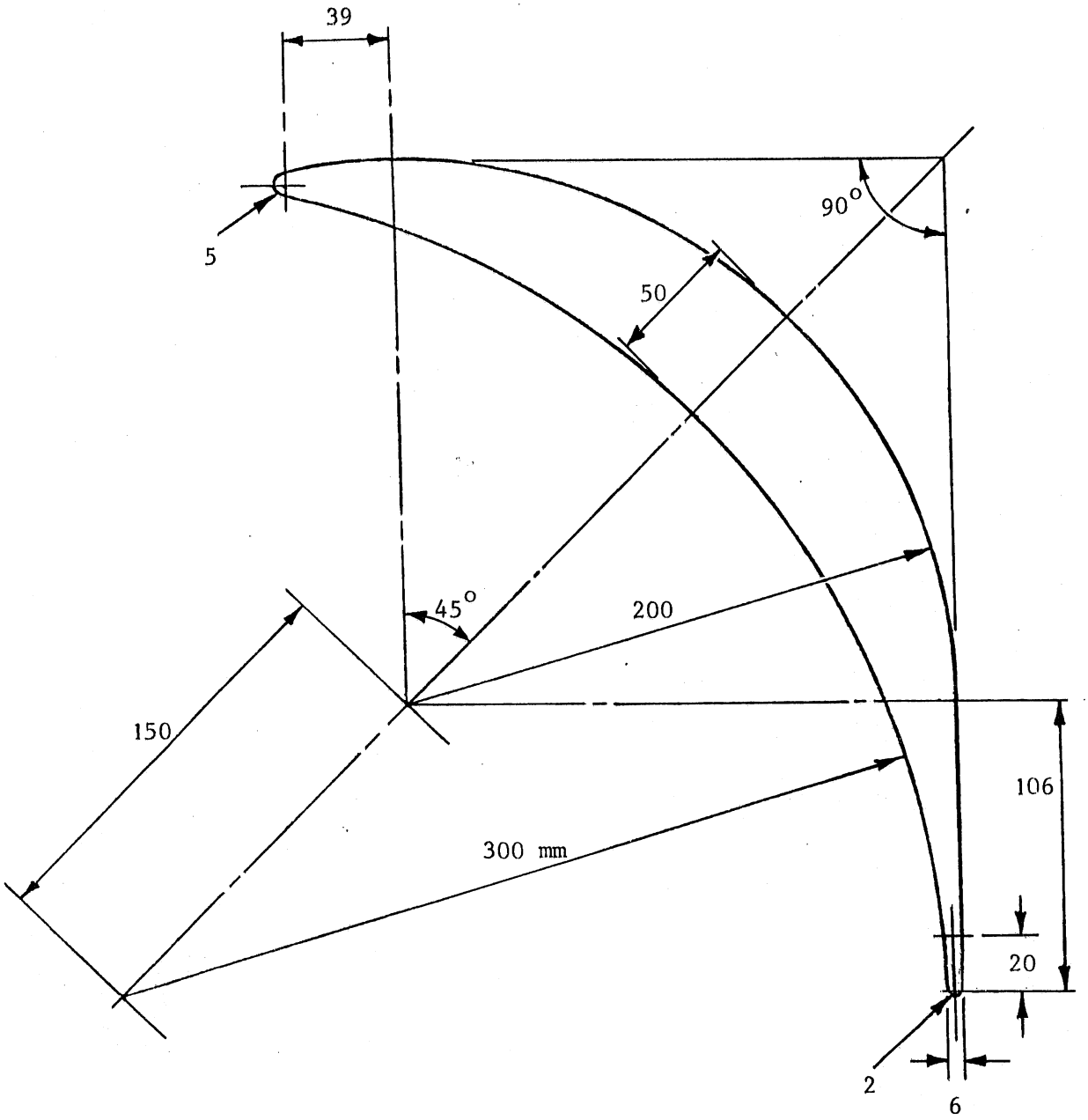

Figure 13. K&R (III,IV) guide vane profile.

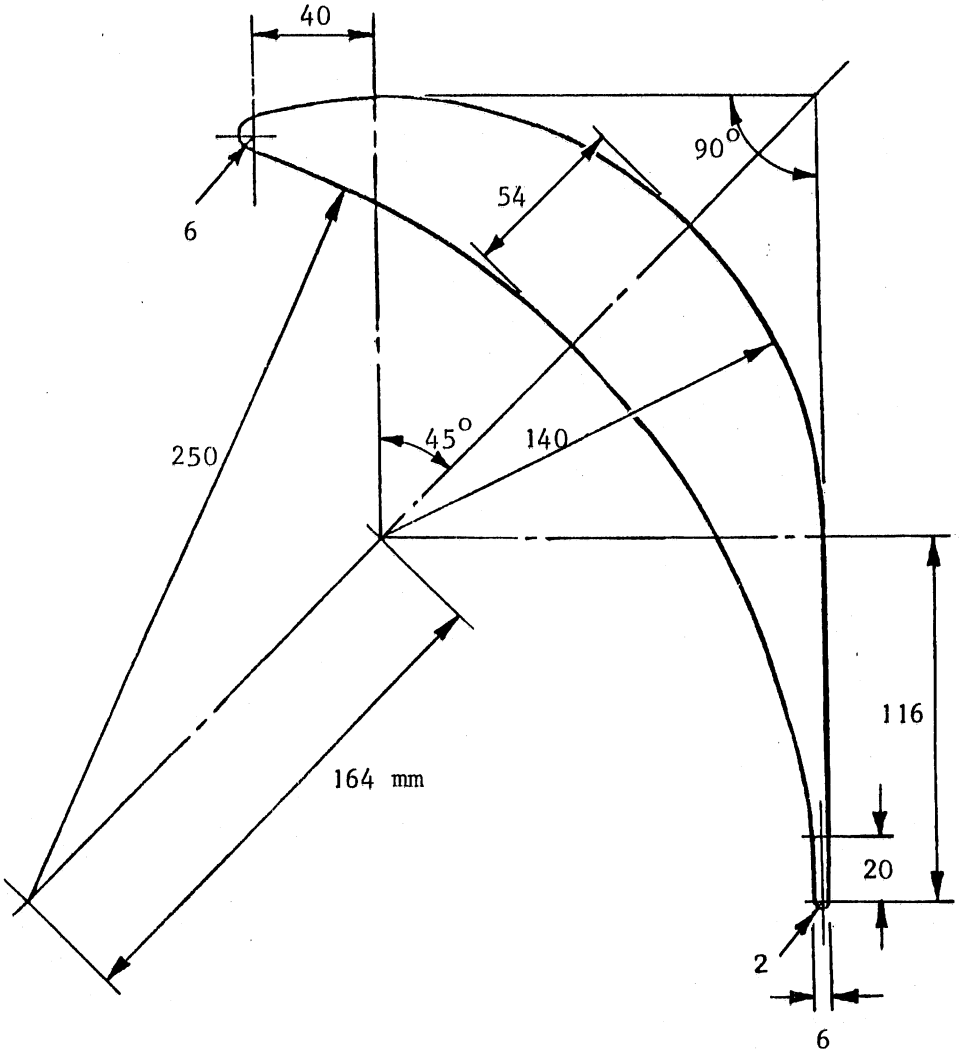

Figure 14. K&R (I,II) guide vane profile.

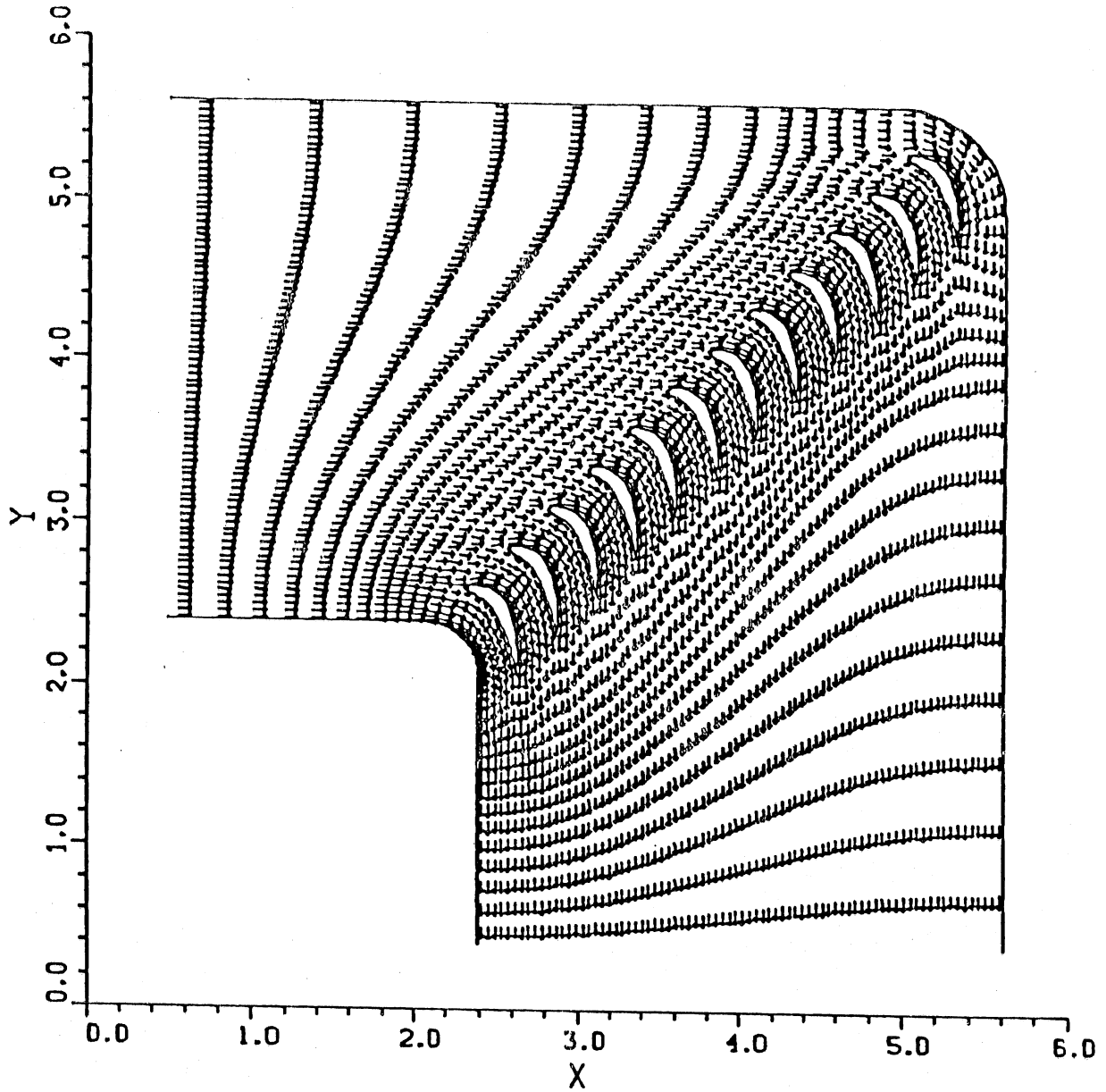

Figure 15. Velocity vector field for NACA (20)315 vanes at normal position.

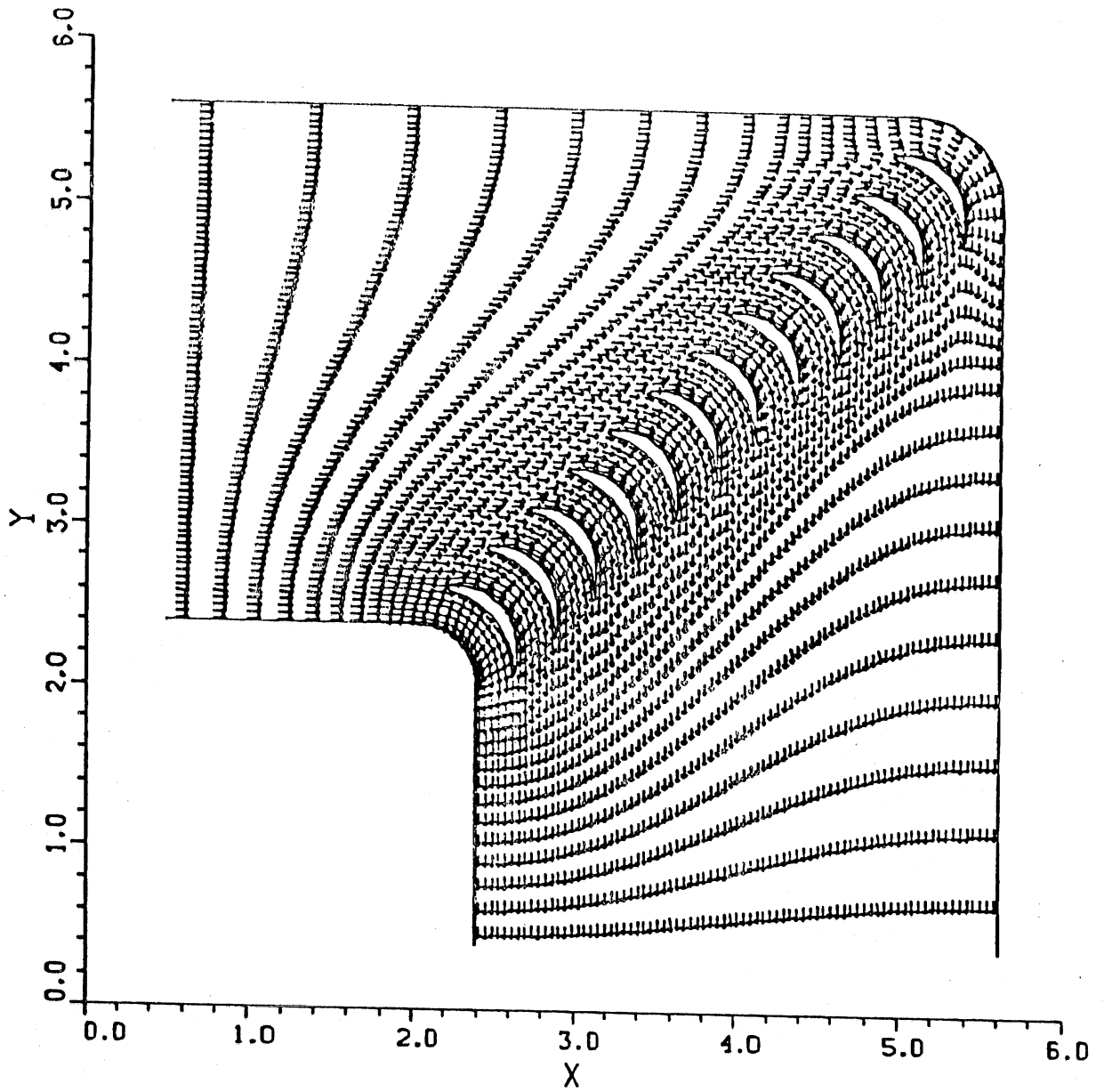

Figure 16. Velocity vector field for K&R (III,IV) vanes at normal position.

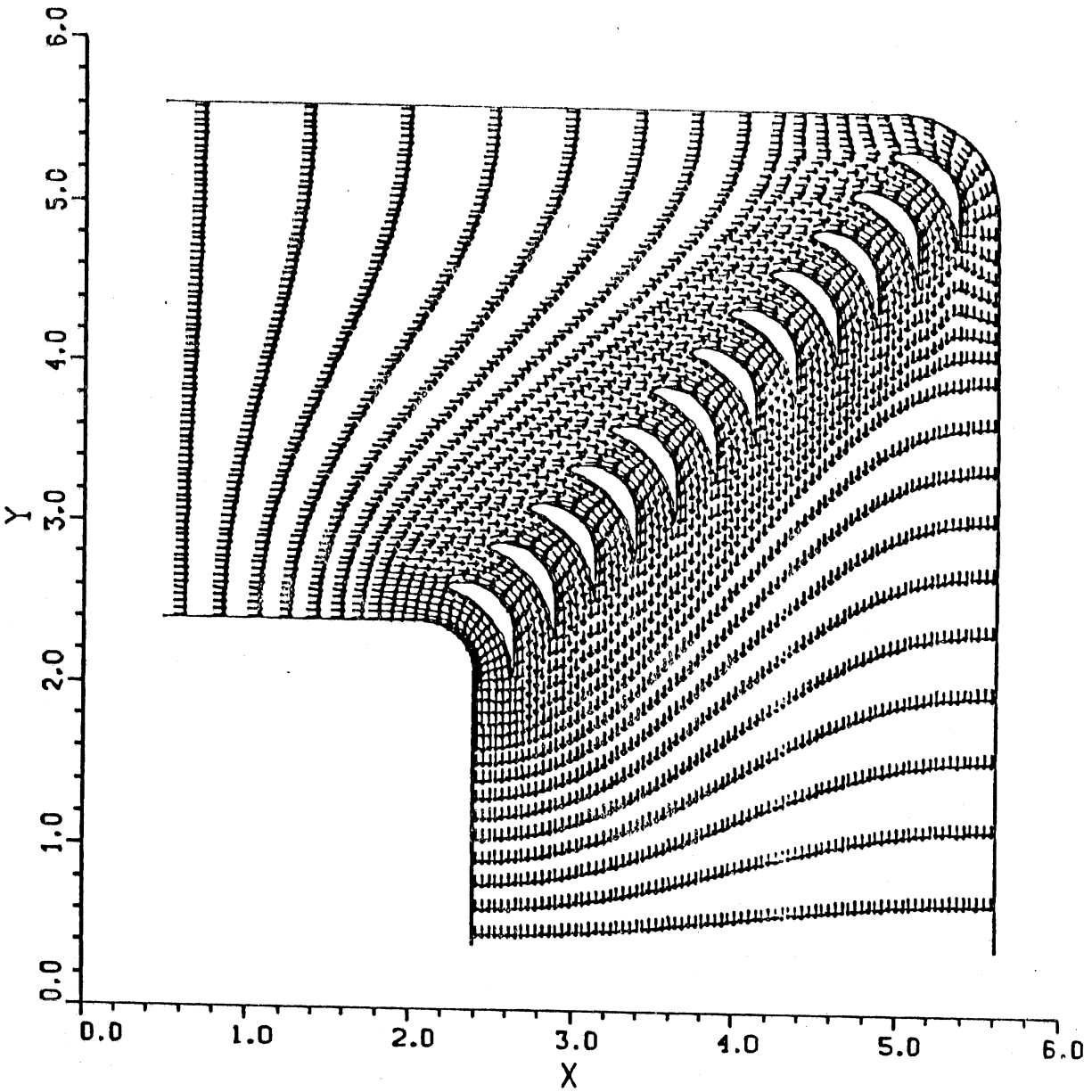

Figure 17. Velocity vector field for K&R (I,III) vanes at normal position.

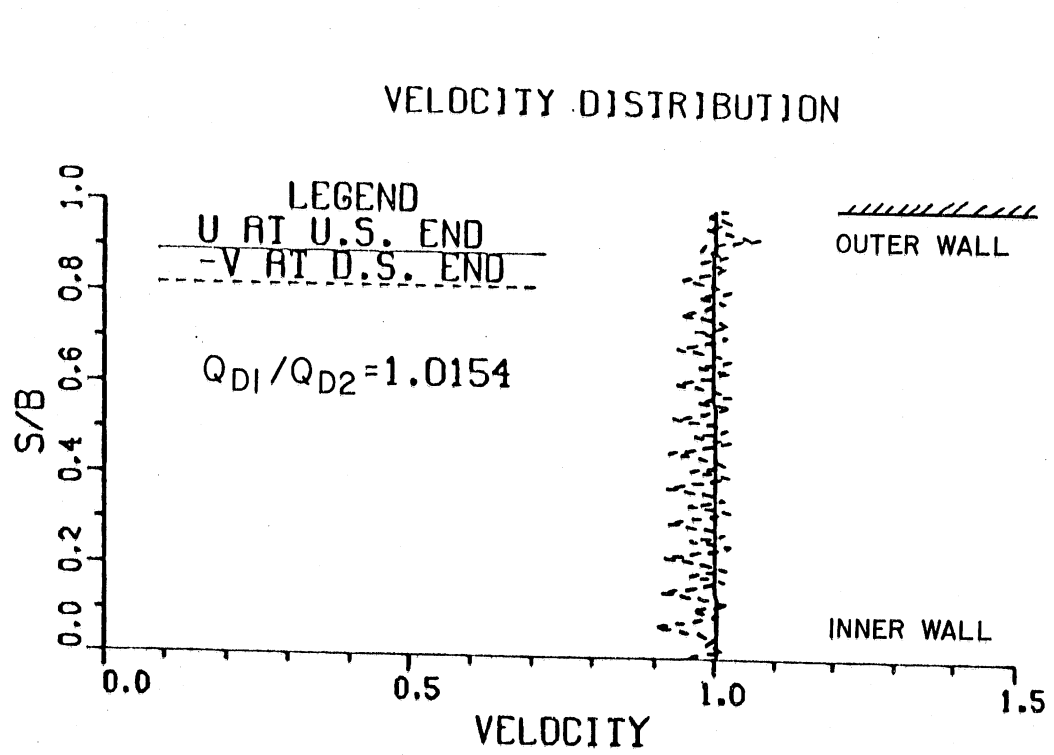

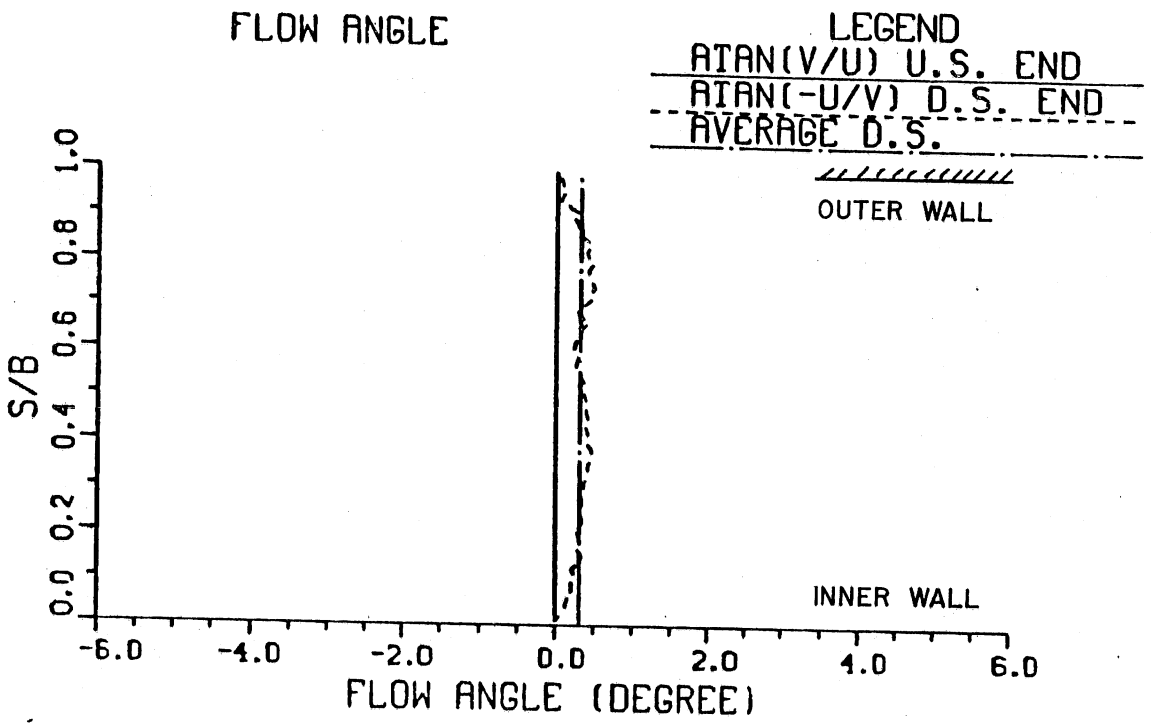

Figure 18. Exit velocity distribution of NACA (20)325 vanes at normal position.

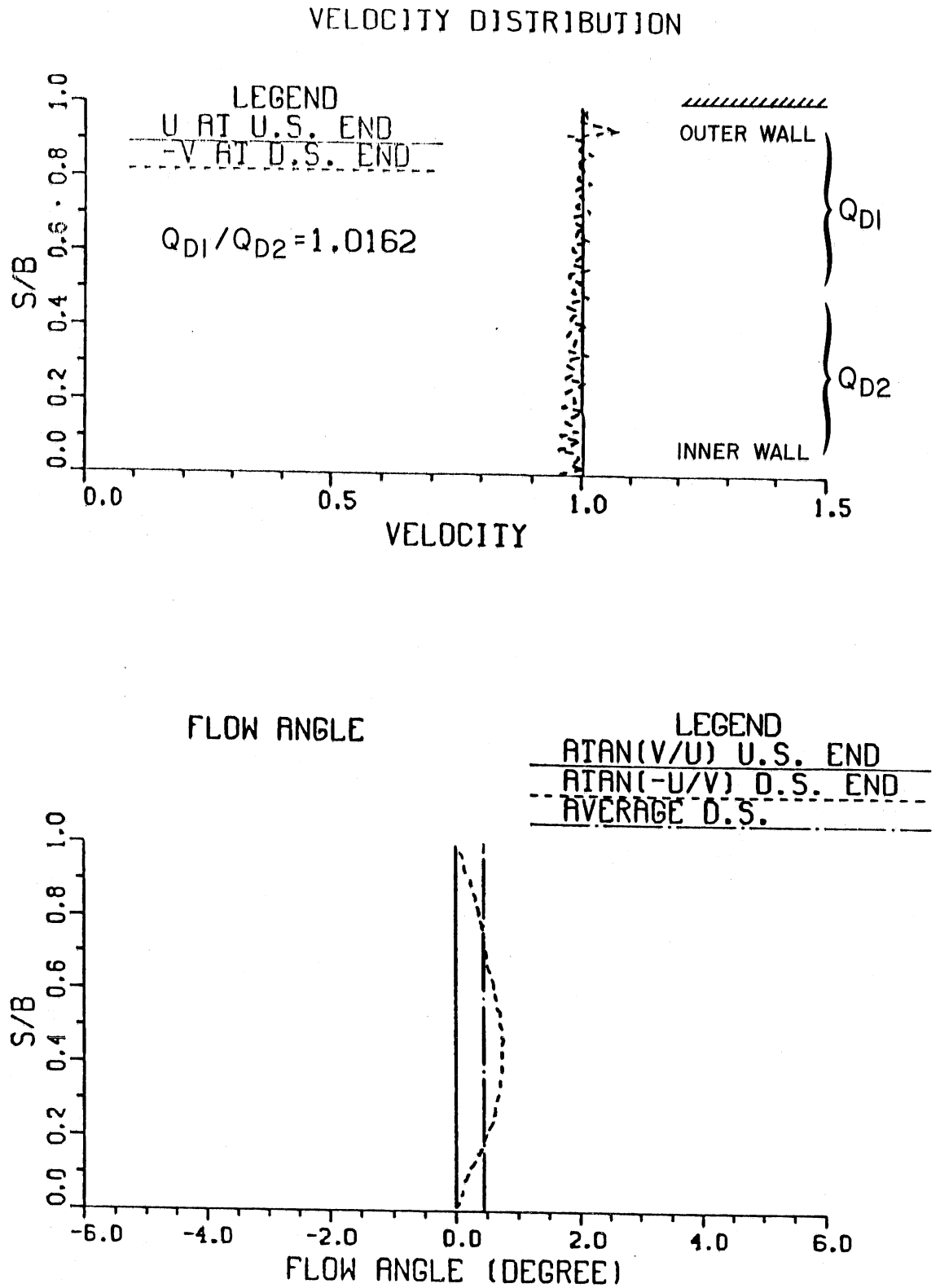

Figure 19. Exit velocity distribution of K&R (III,IV) vanes at normal position.

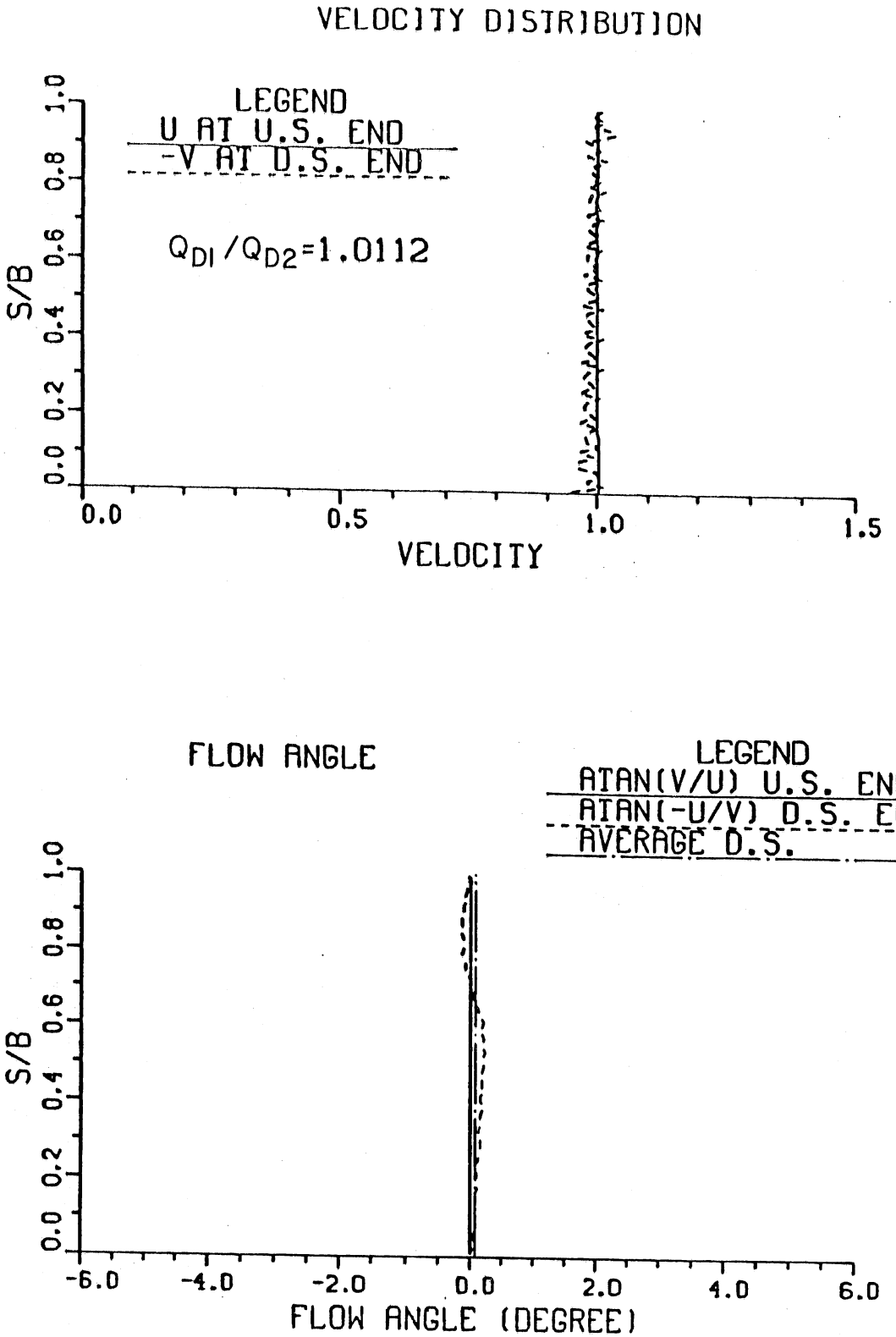

Figure 20. Exit velocity distribution of K&R (I,II) vanes at normal position.

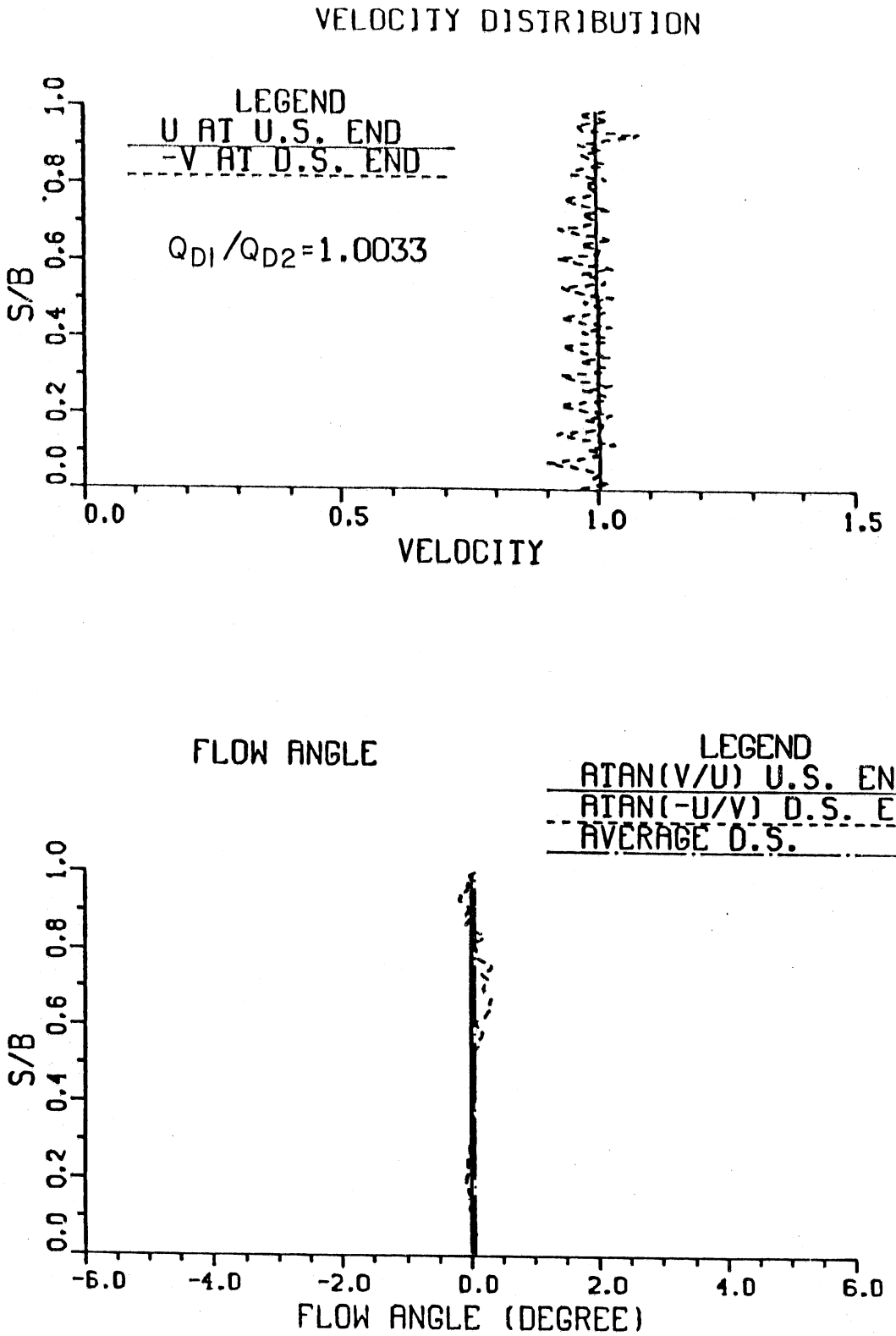

Figure 21. Exit velocity distribution of NACA (20)325 vanes rotated 1 degree.

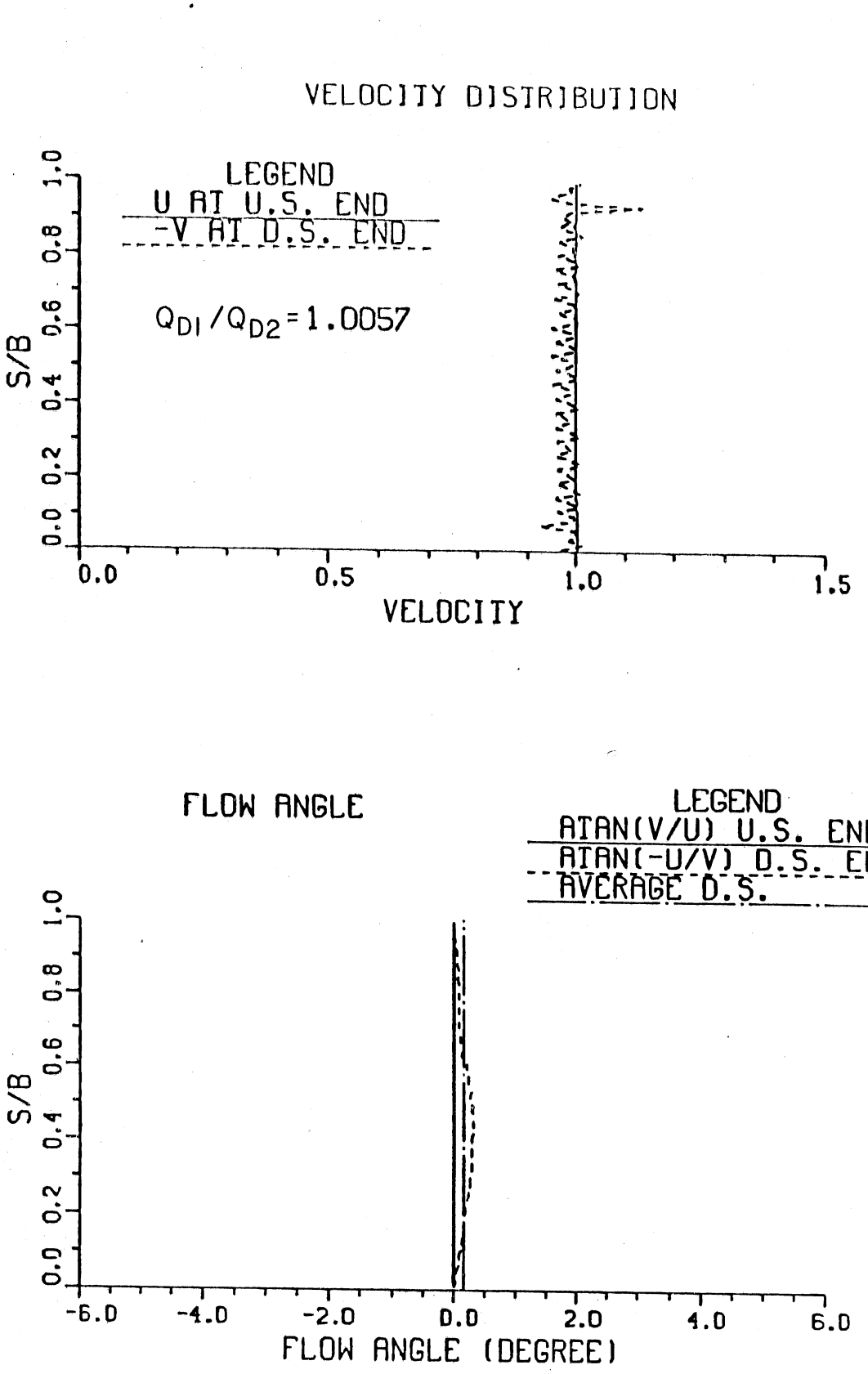

Figure 22. Exit velocity distribution of K&R (III,IV) vanes rotated 1.5 degrees.

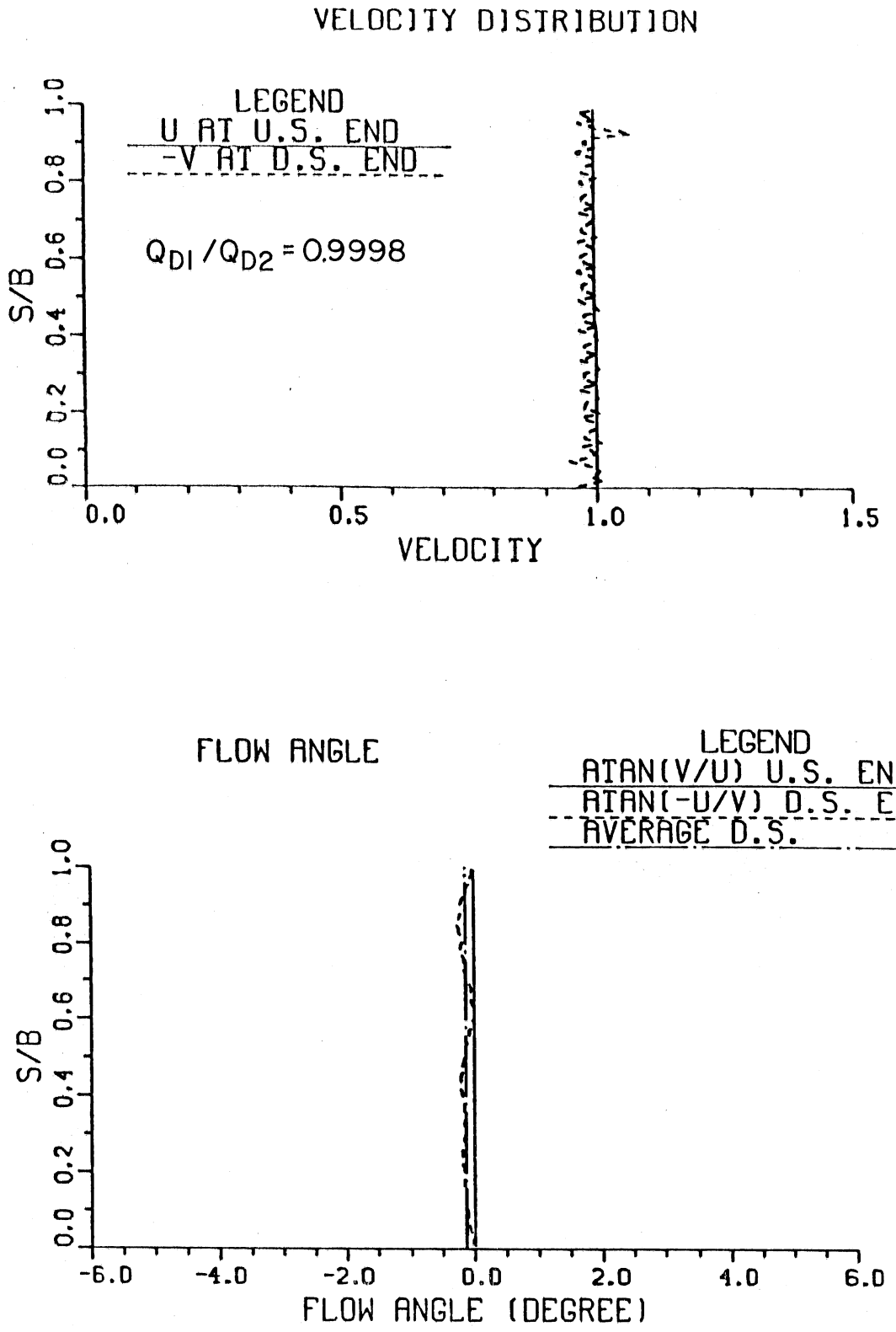

Figure 23. Exit velocity distribution of K&R (I,II) vanes rotated 0.5 degrees.

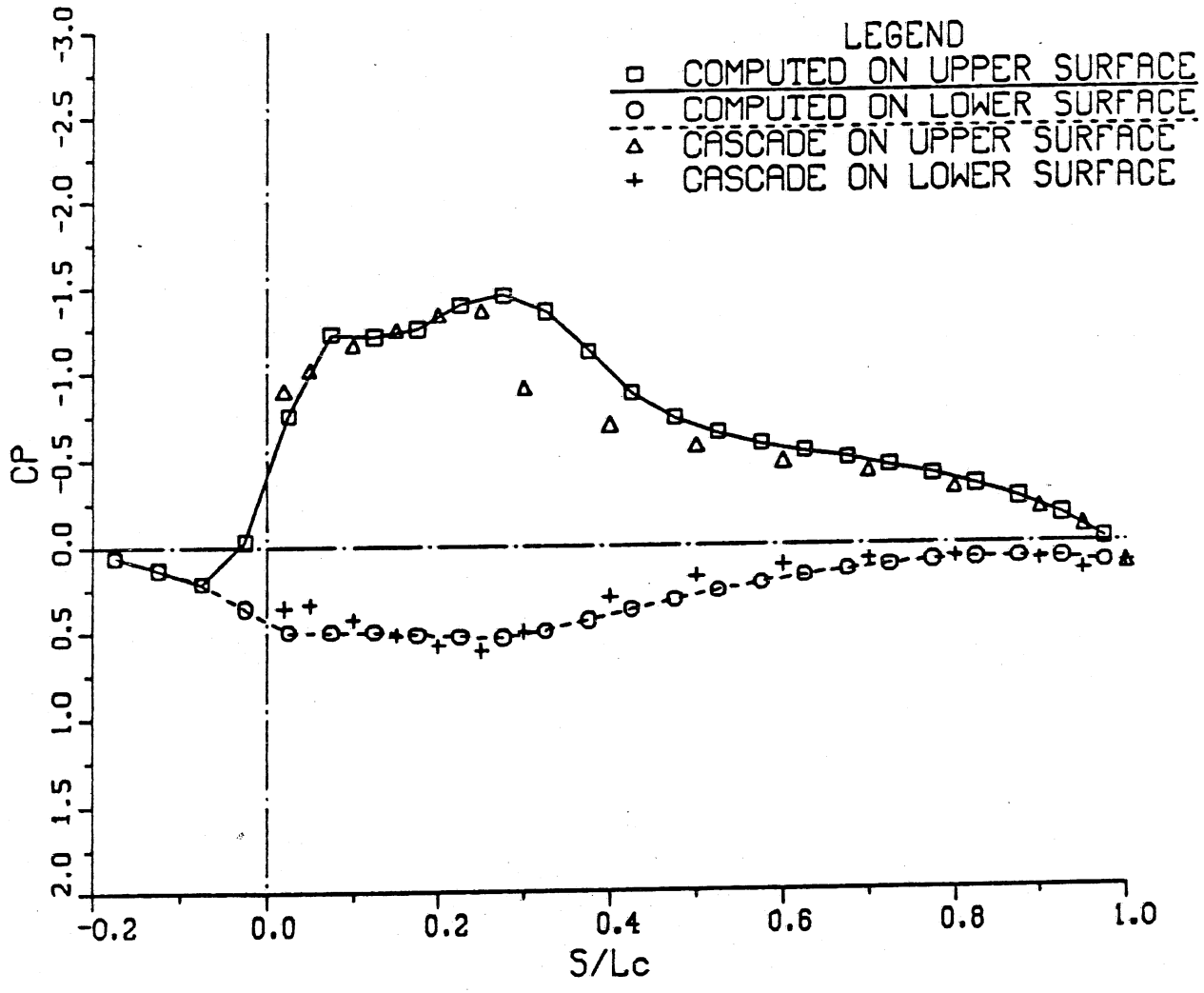

Figure 24. Pressure distribution on inner vane for NACA (20)315 vane at normal position computed with coarse grid system.

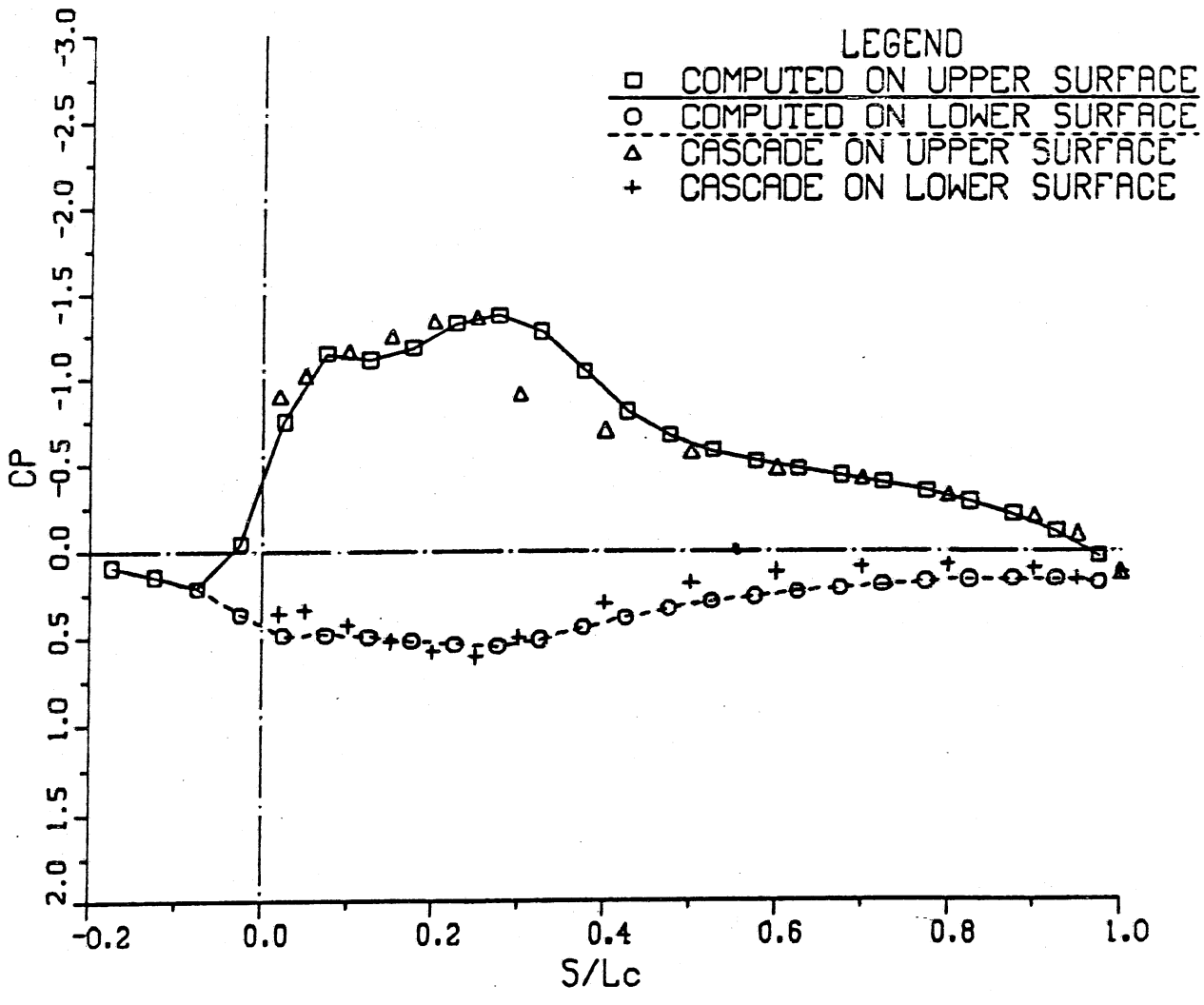

Figure 25. Pressure distribution on center vane for NACA (20)315 vane at normal position computed with coarse grid system.

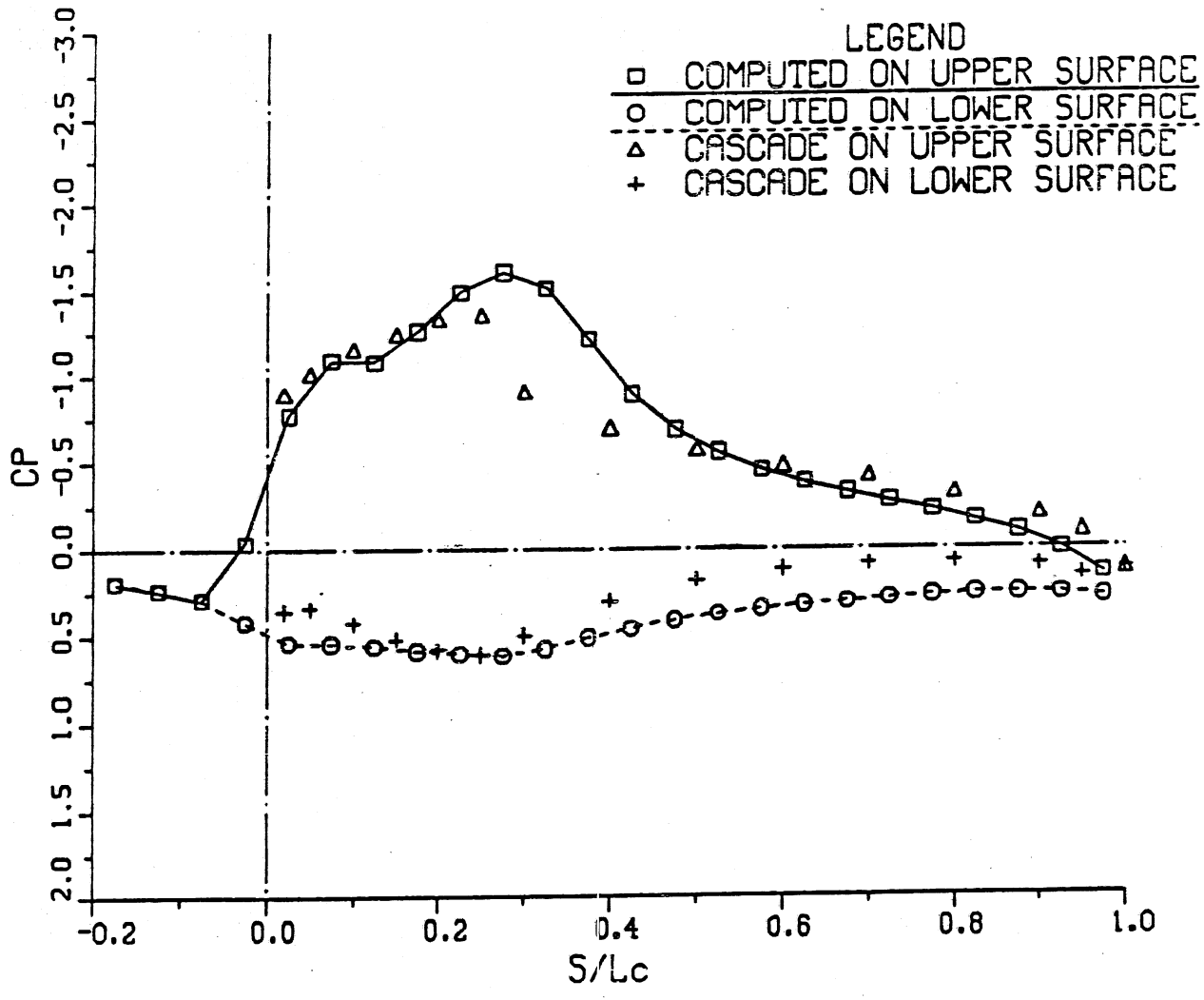

Figure 26. Pressure distribution on outer vane for NACA (20)315 vane at normal position computed with coarse grid system.

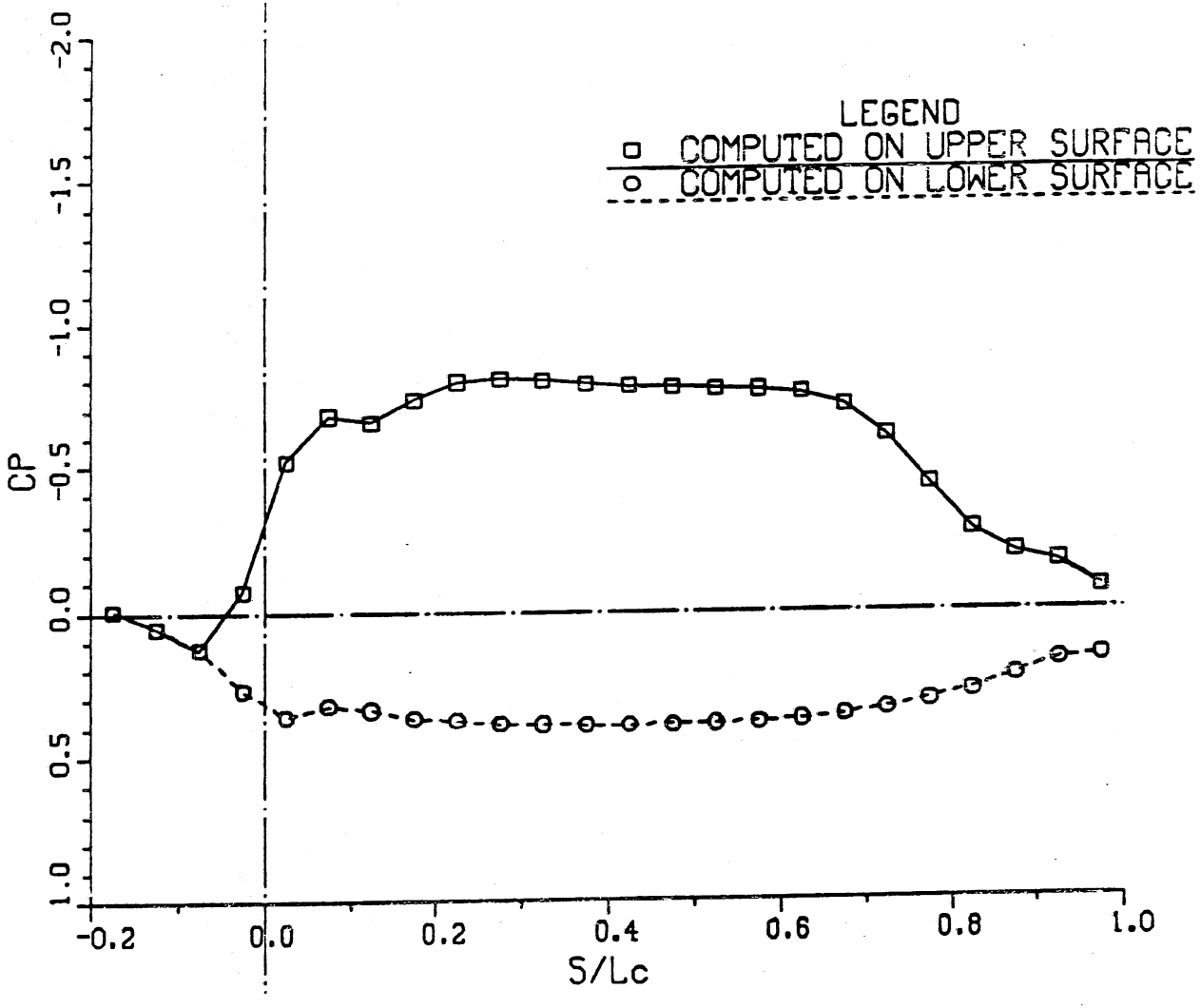

Figure 27. Pressure distribution on inner K&R (III,IV) vane.

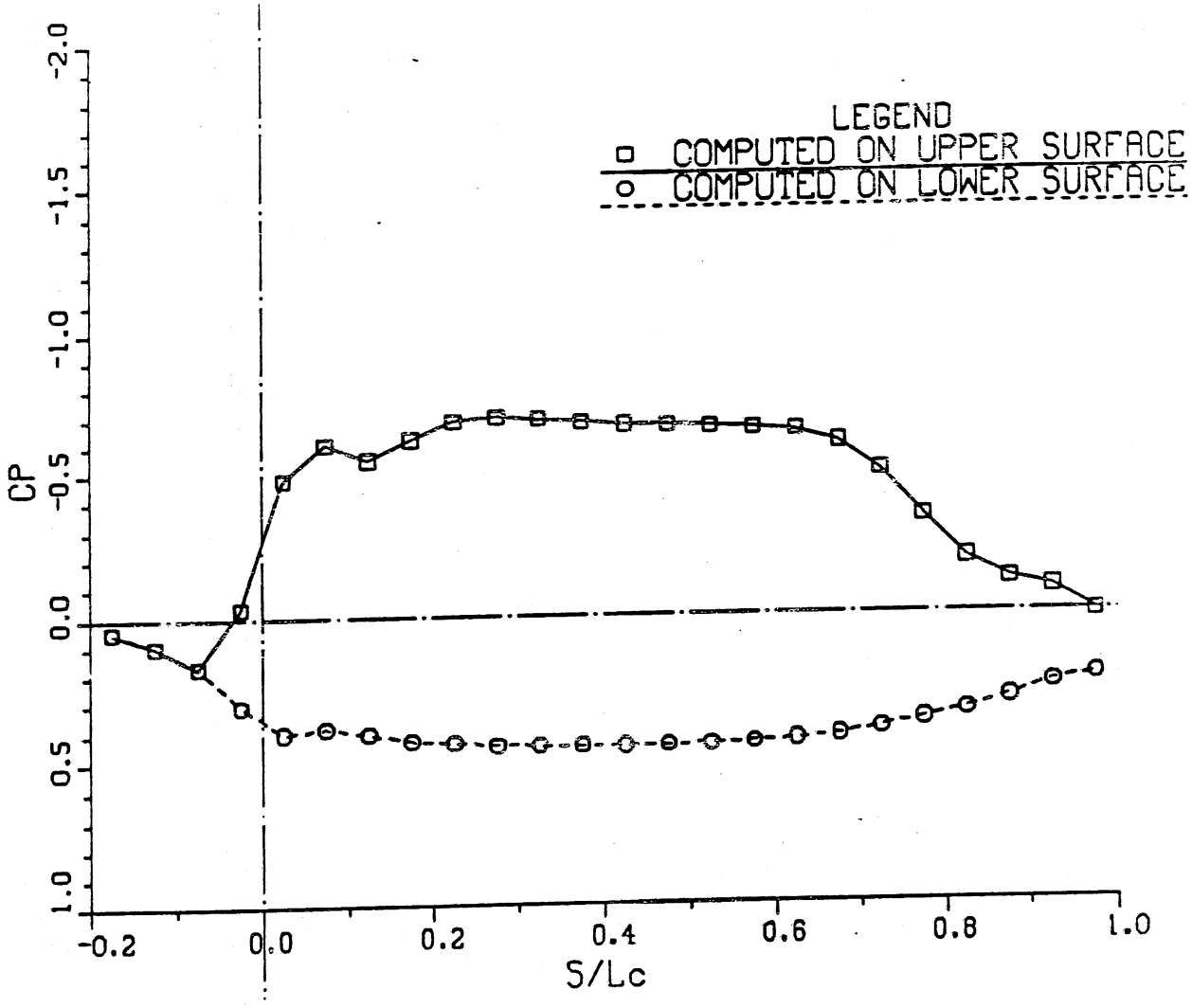

Figure 28. Pressure distribution on center K&R (III,IV) vane.

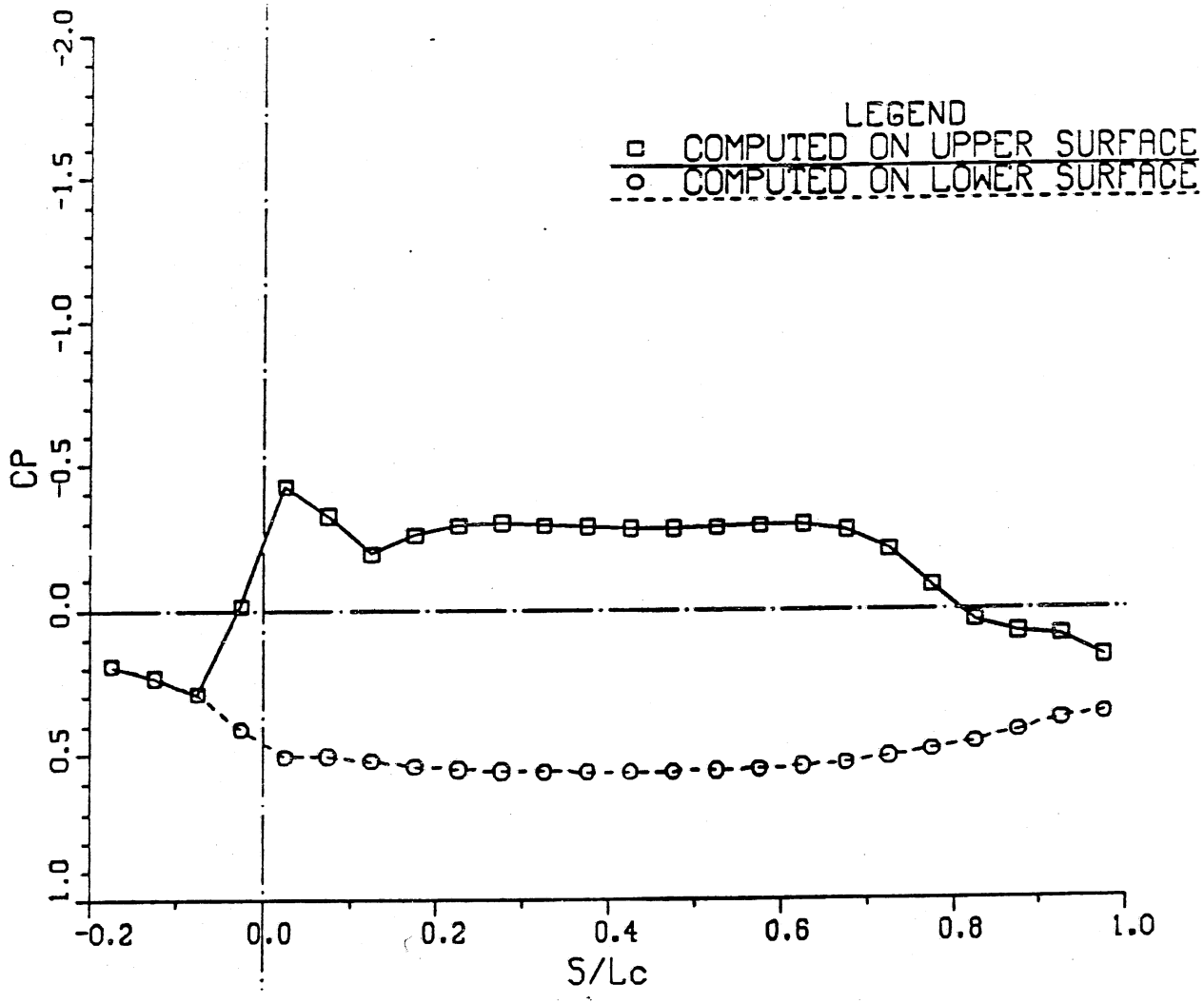

Figure 29. Pressure distribution on outer K&R (III,IV) vane.

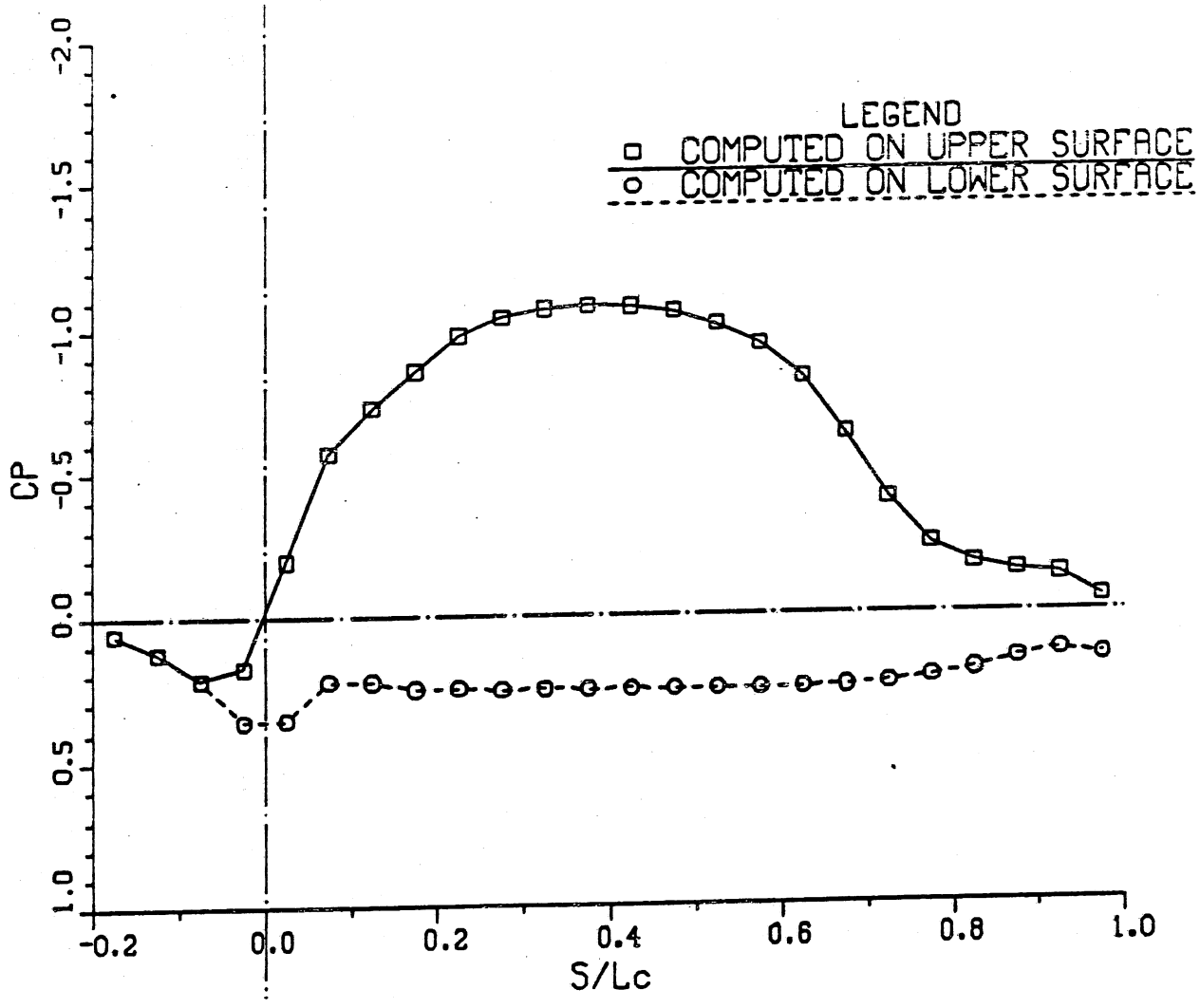

Figure 30. Pressure distribution on inner K&R (I,II) vane.

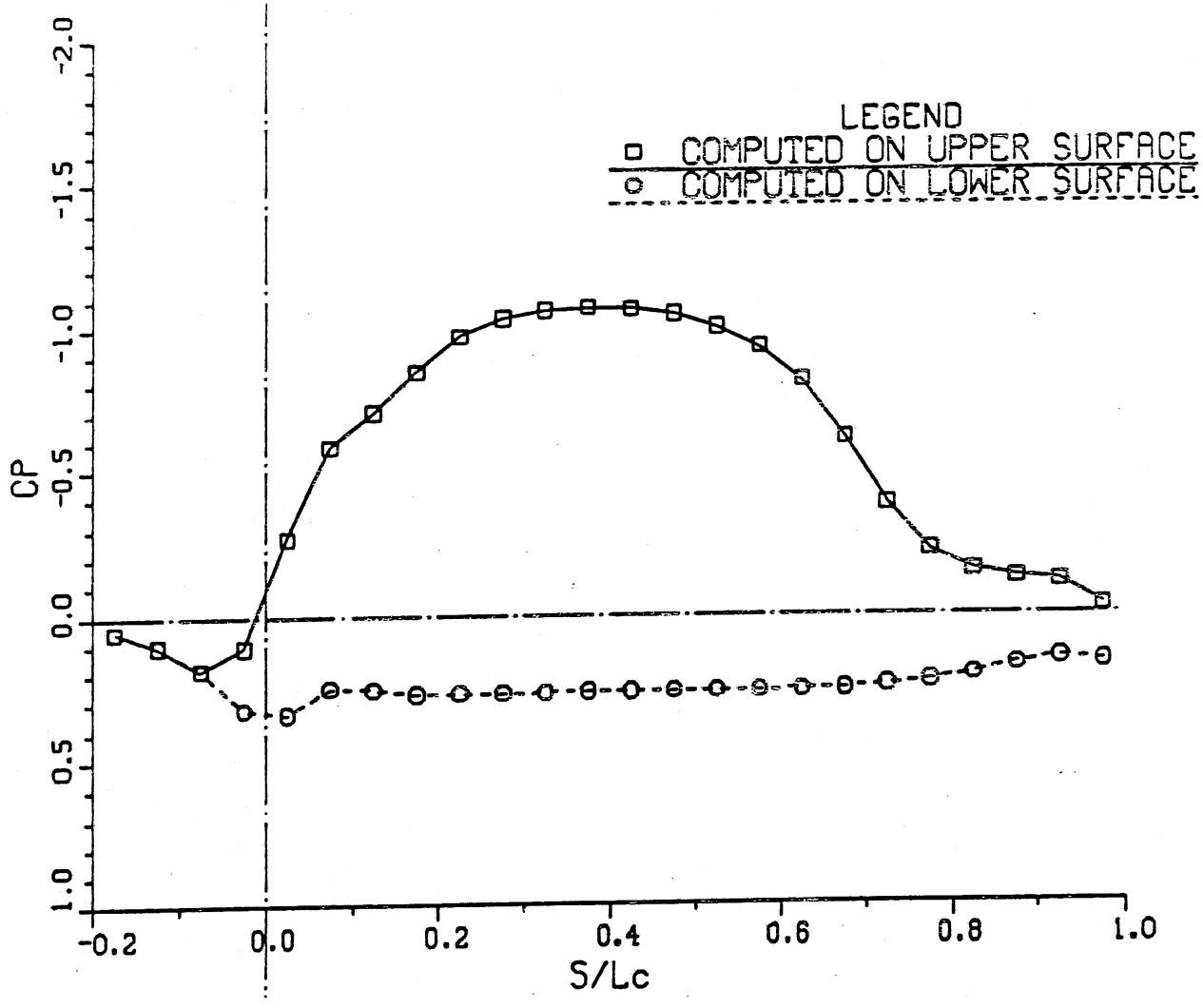

Figure 31. Pressure distribution on center K&R (I,II) vane.

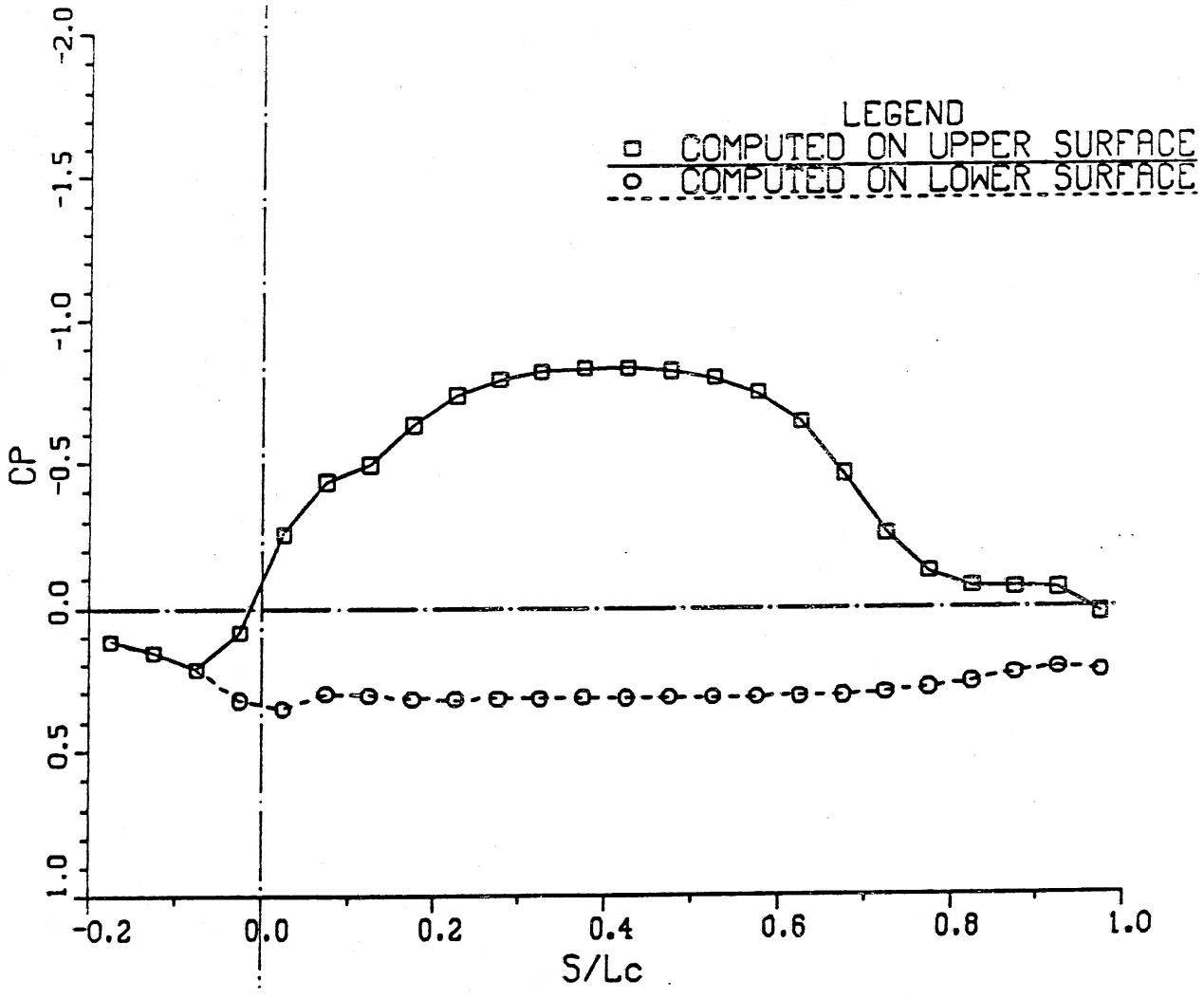

Figure 32. Pressure distribution on outer K&R (I,II) vane.

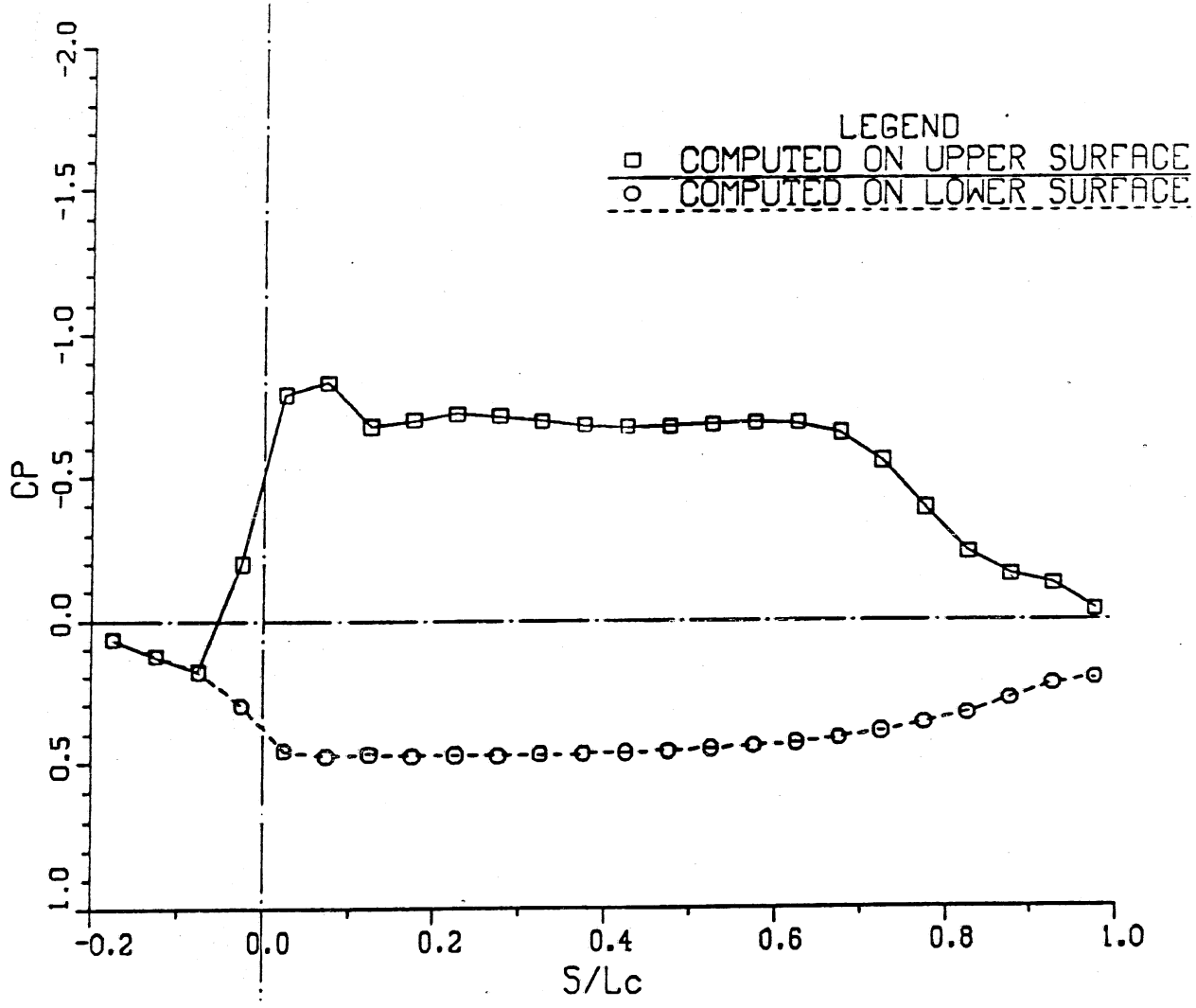

Figure 33. Pressure distribution on inner K&R (III,IV) vane at 1.5 degrees overturned position.

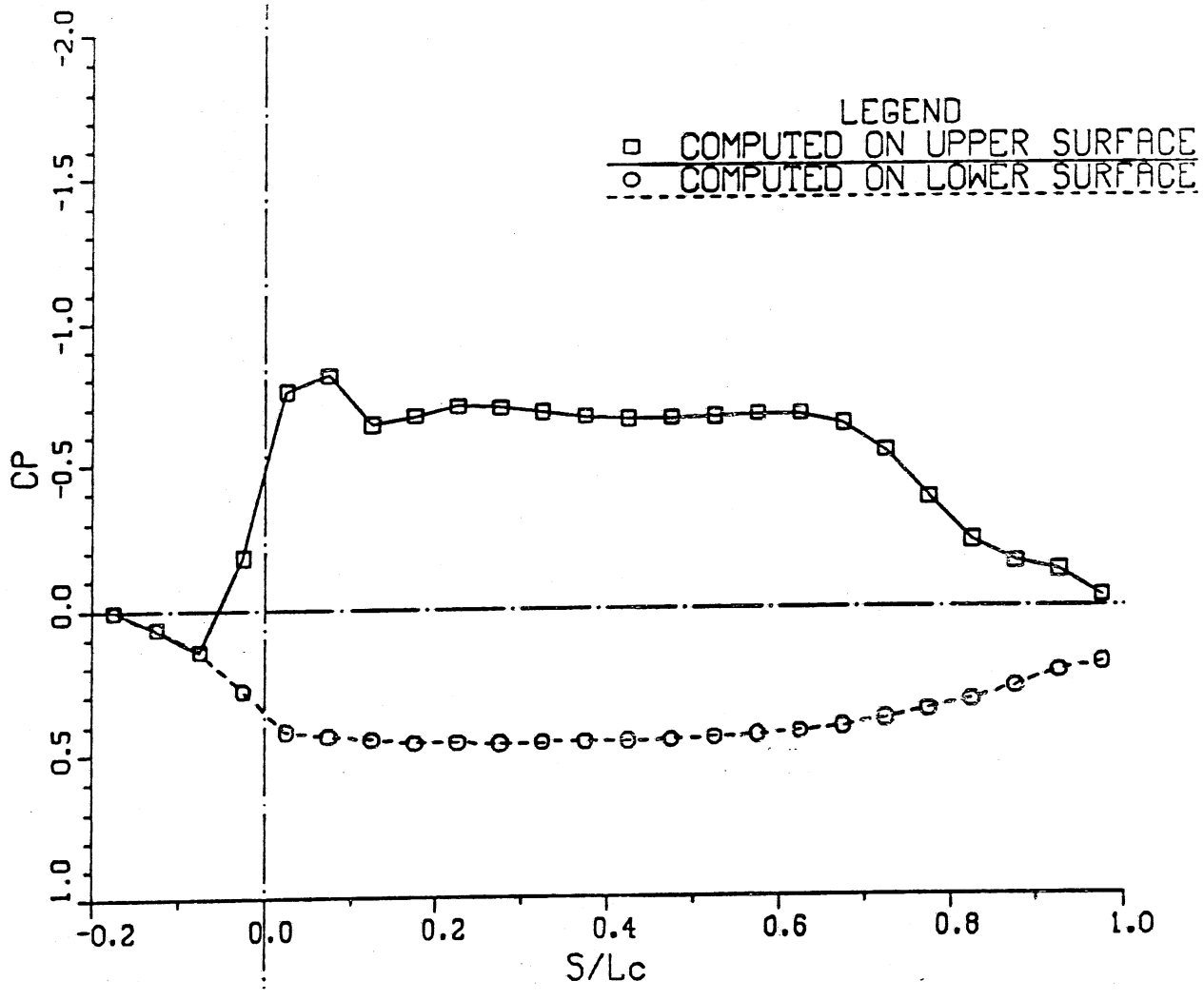

Figure 34. Pressure distribution on center K&R (III,IV) vane at 1.5 degrees overturned position.

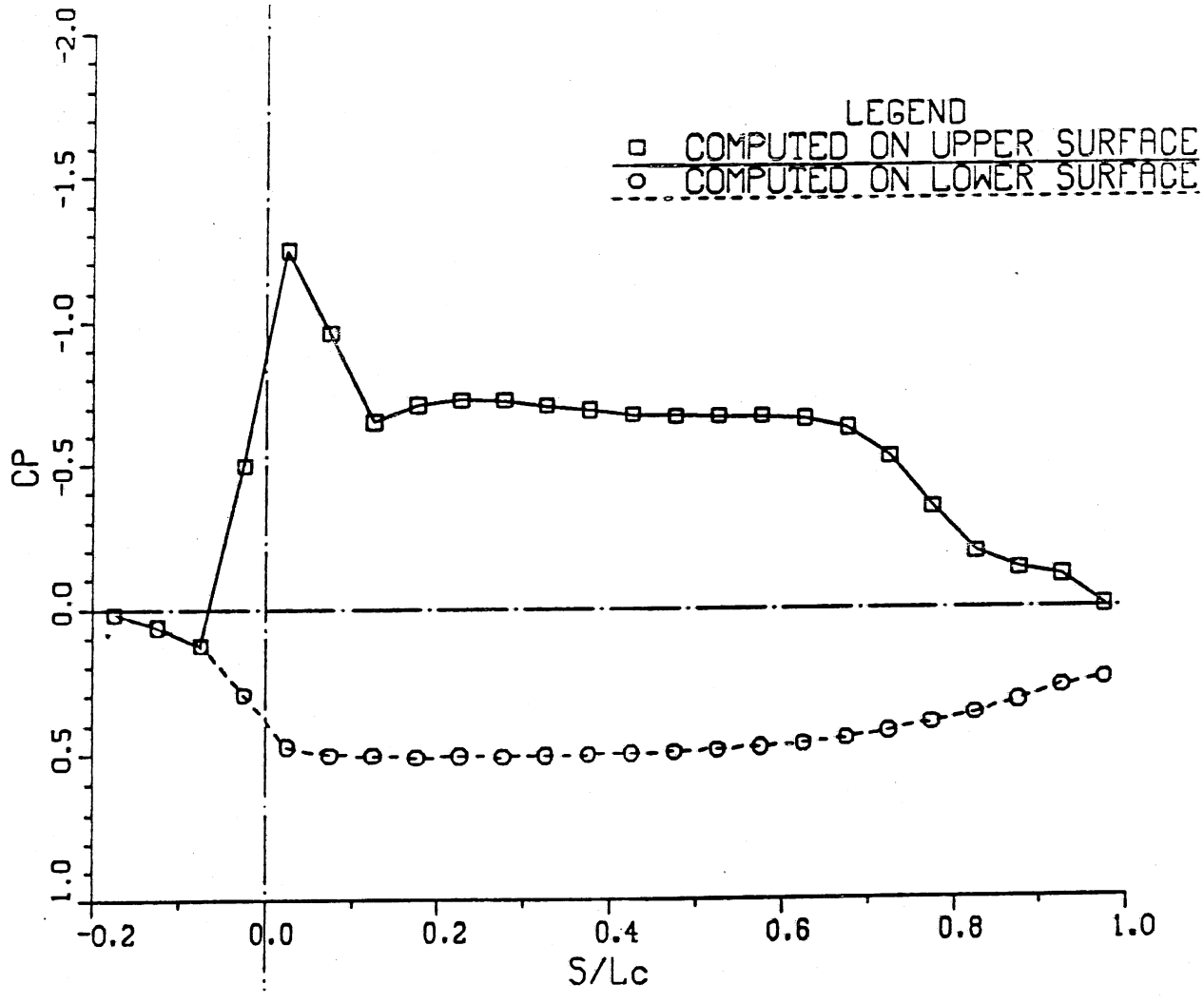

Figure 35. Pressure distribution on outer K&R (III,IV) vane at 1.5 degrees overturned position.

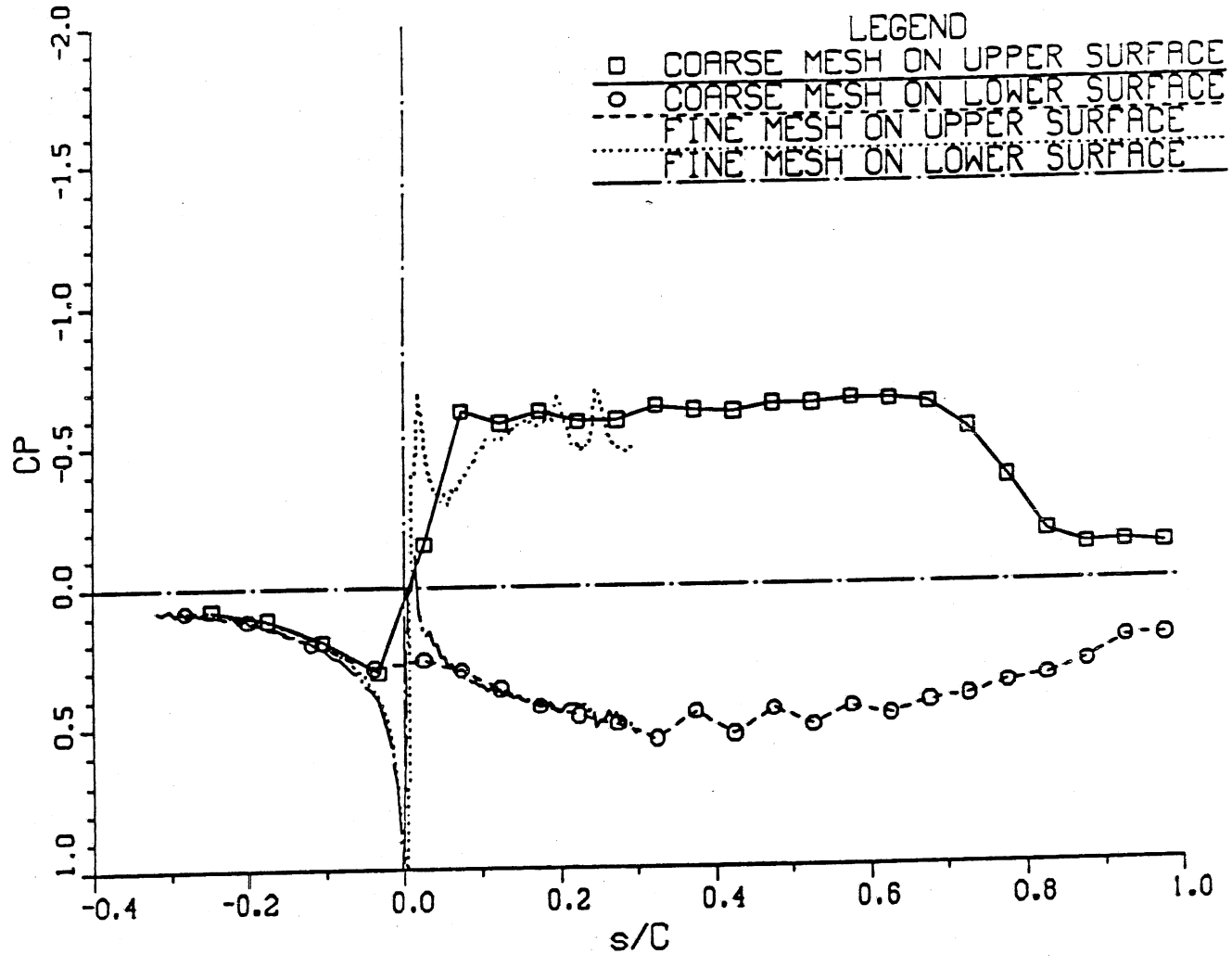

Figure 36. Pressure distribution on center K&R (III,IV) vane at 1.5 degrees overturned position, a 1/25 nested grid system.

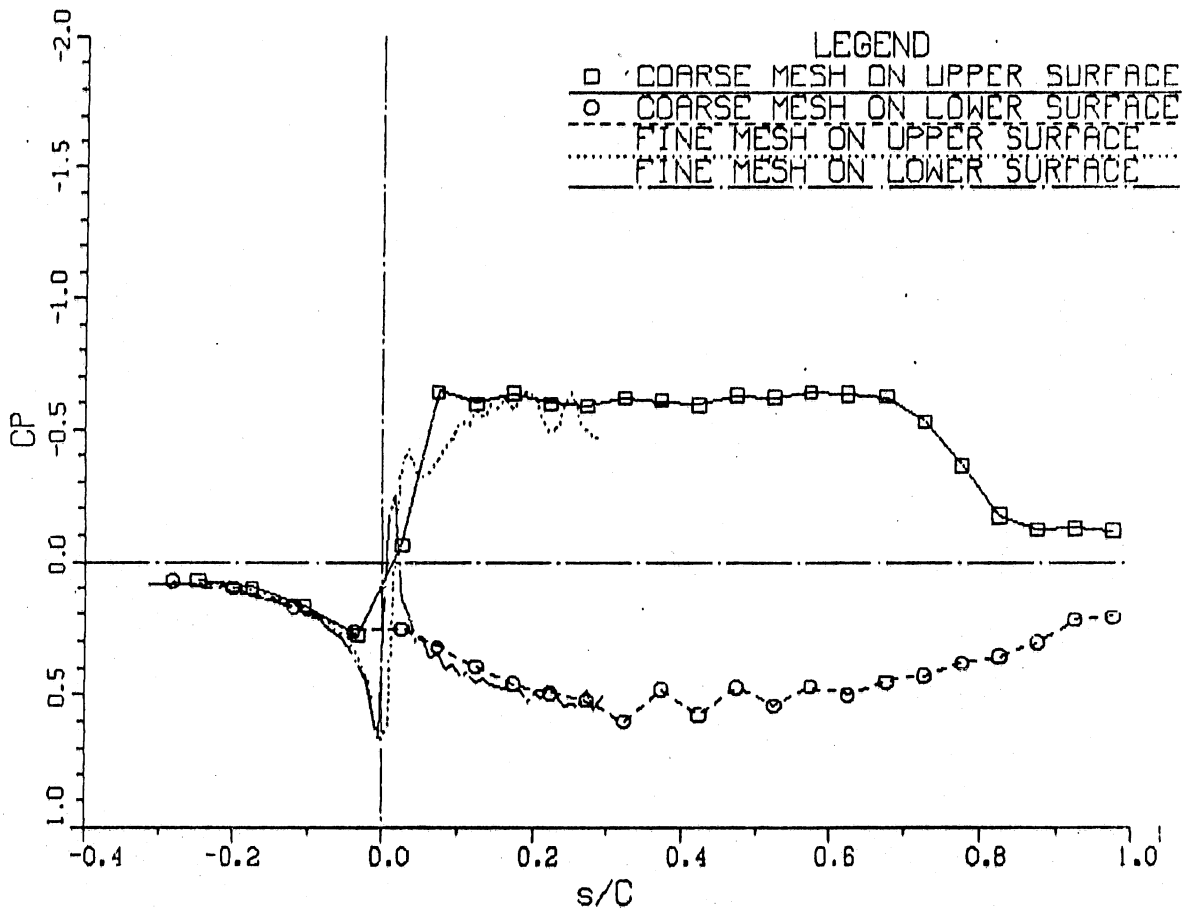

Figure 37. Pressure distribution on center K&R (III,IV) vane at 1.5 degrees overturned position, a 1/100 nested grid system.

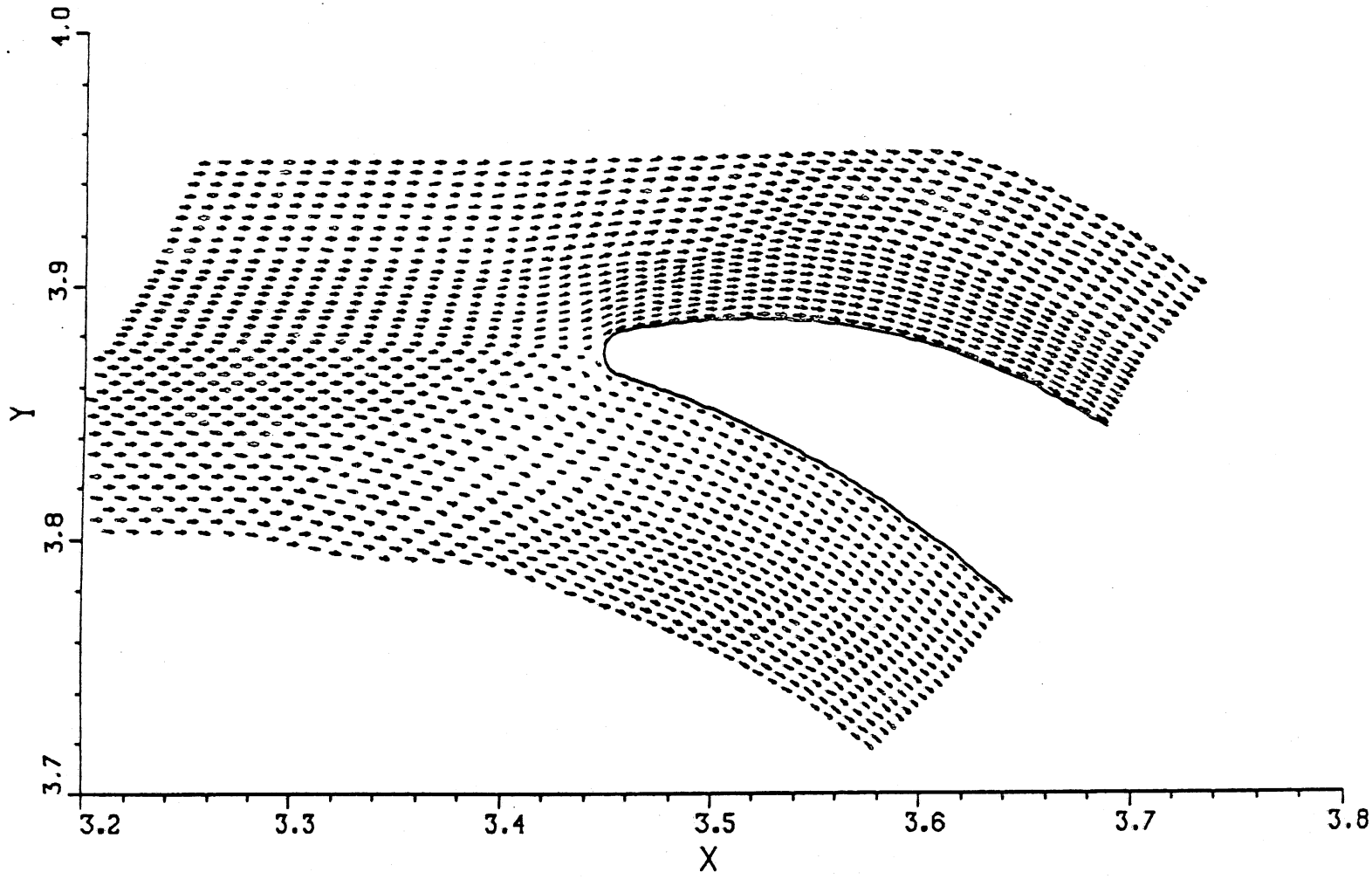

Figure 38. Velocity vector field on center K&R (III,IV) vane at 1.5 degrees overturned position, a 1/100 nested grid system.

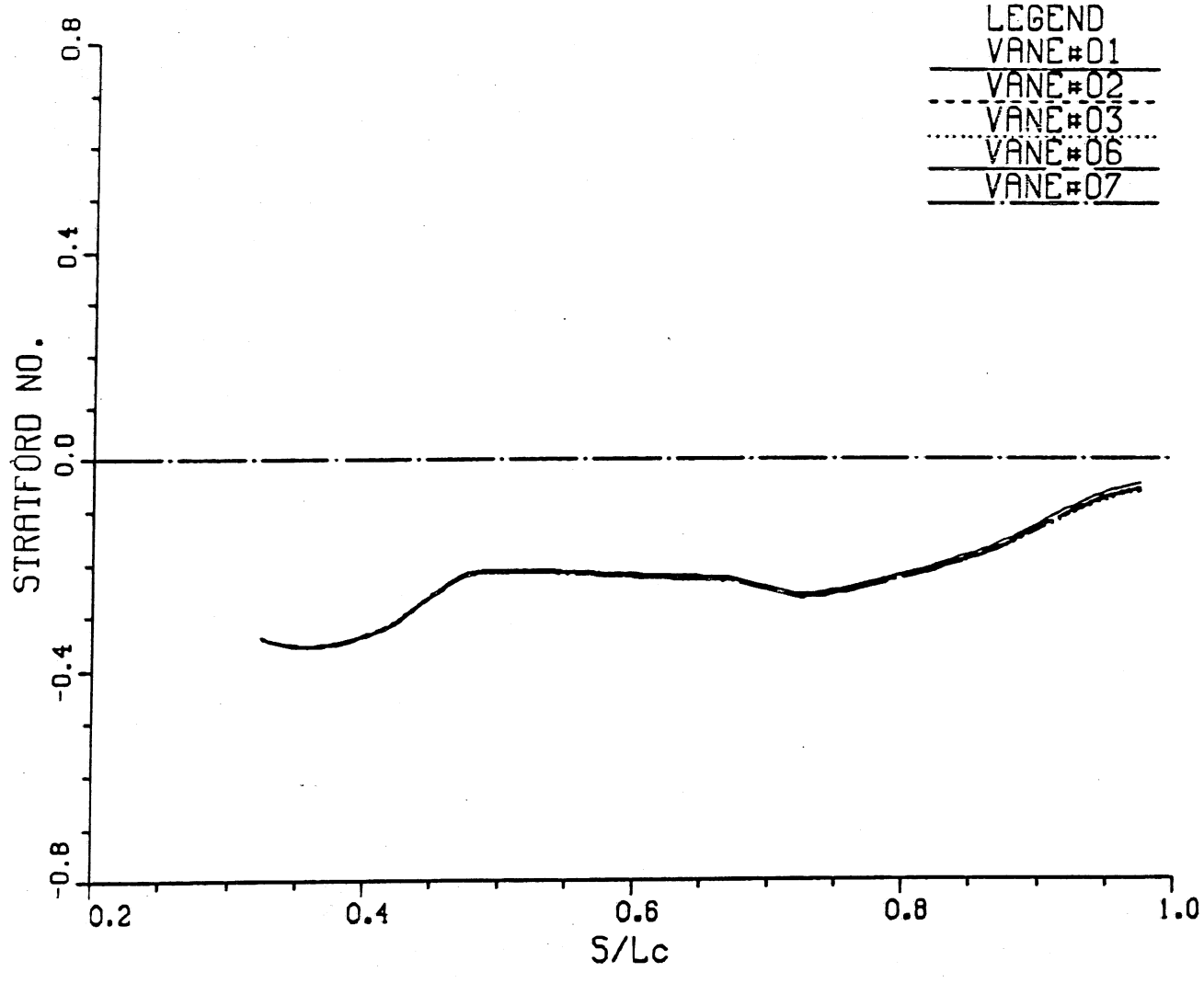

Figure 39. Stratford number distribution along the upper surface of six NACA (20)315 vanes near the inner wall.

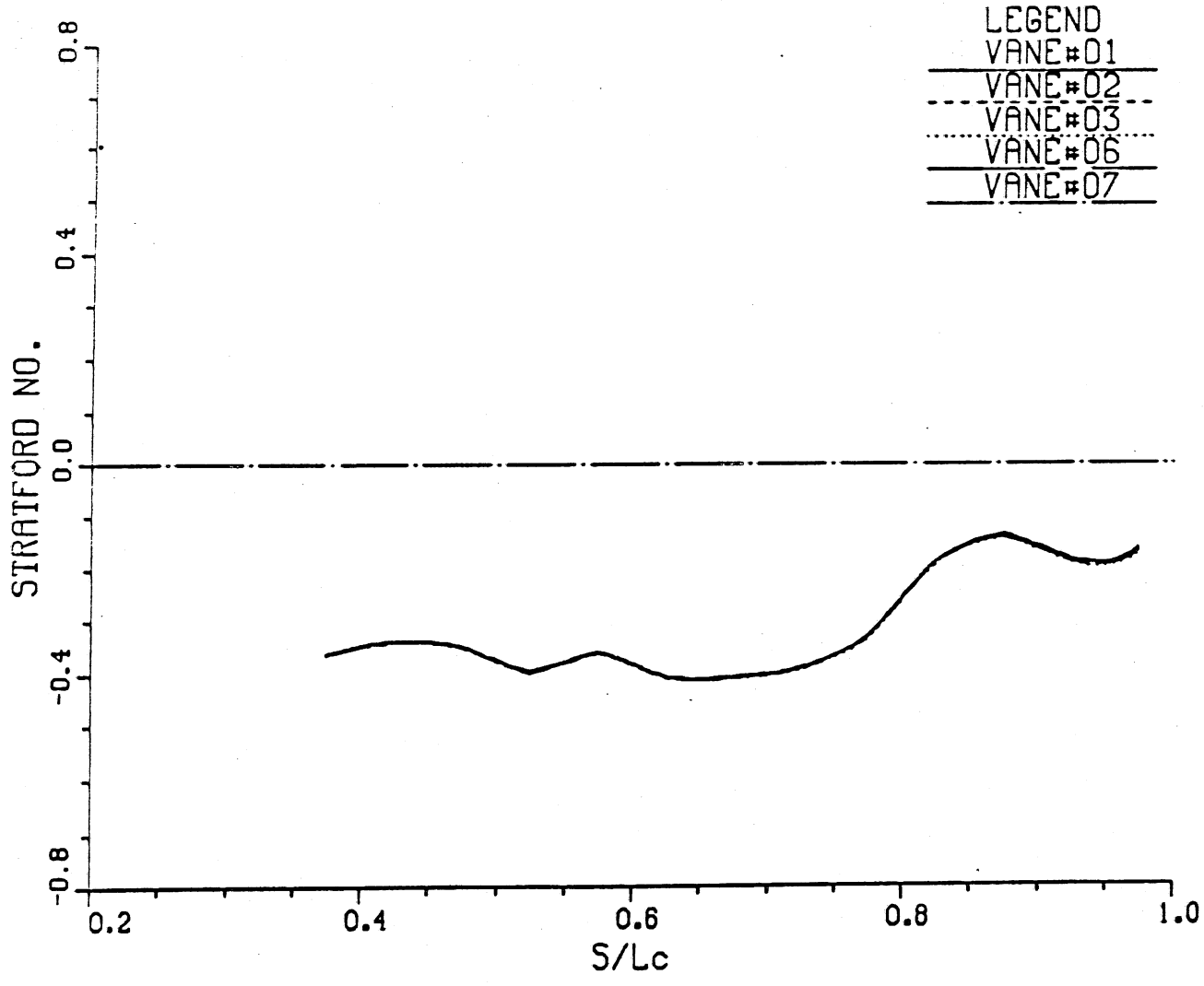

Figure 40. Stratford number distribution along the upper surface of six K&R (III,IV) vanes near the inner wall.

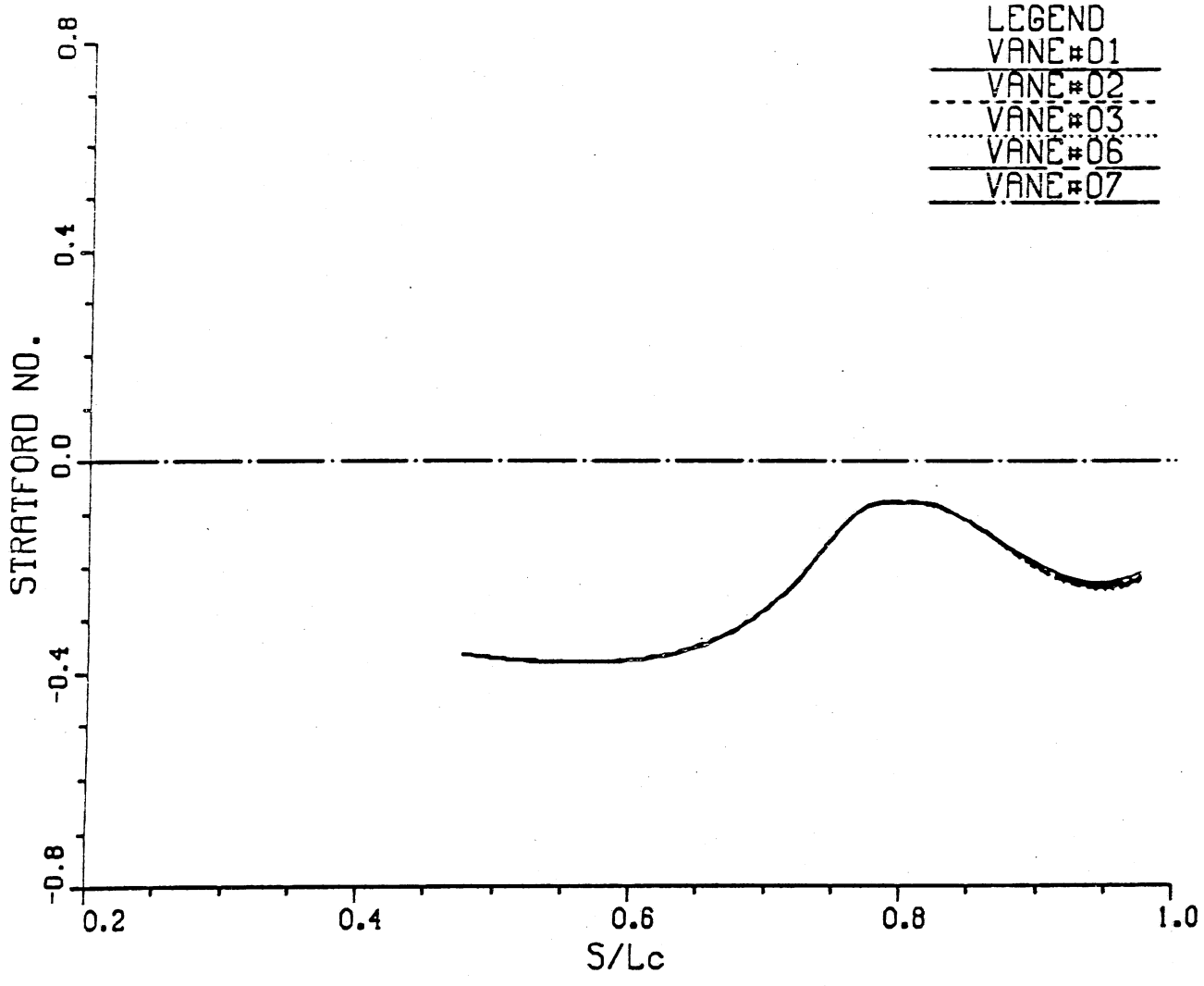

Figure 41. Stratford number distribution along the upper surface of six K&R (I,II) vanes near the inner wall.

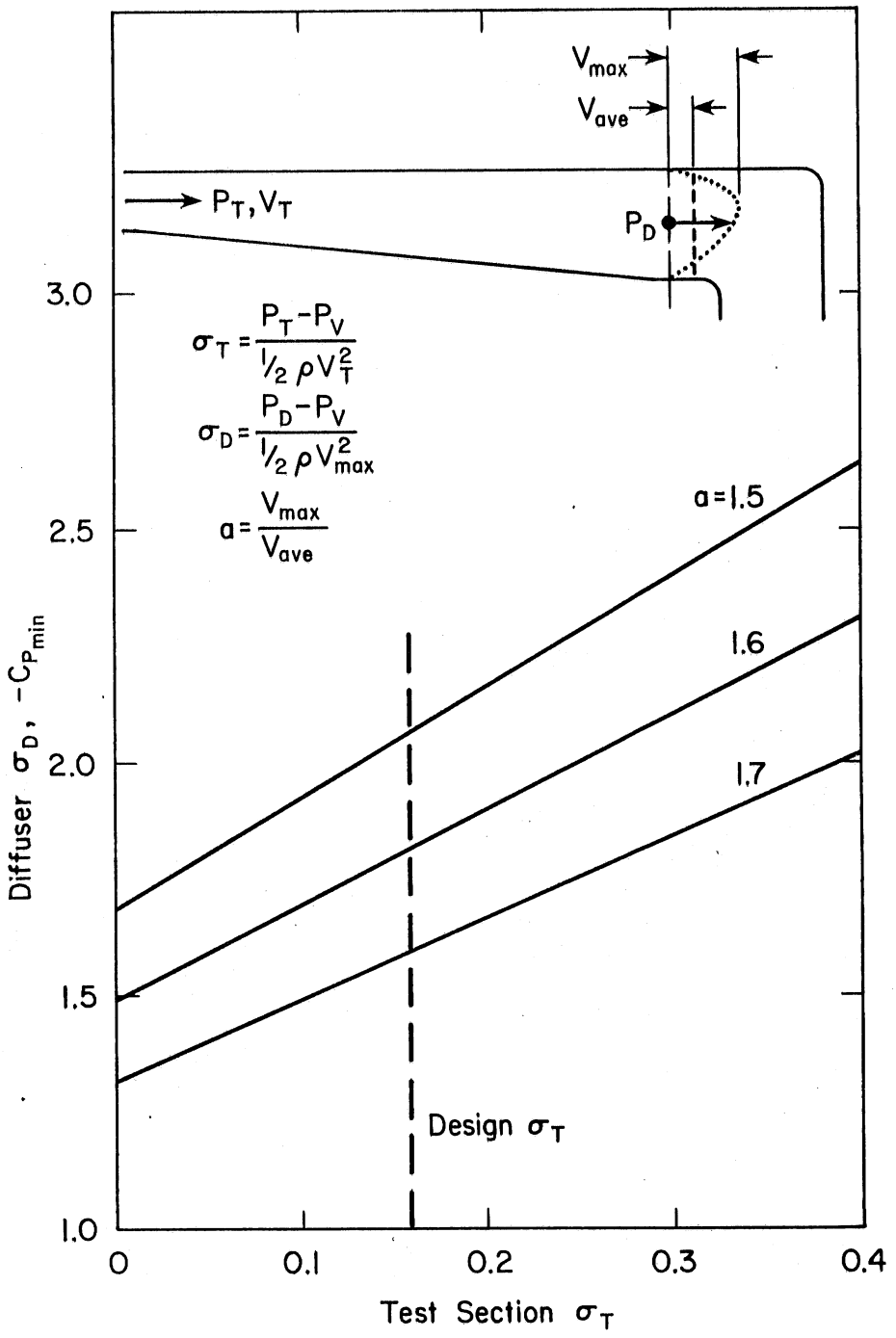

Figure 42. Cavitation susceptibility of turning vanes in first elbow.